



DEFN: Dual-Encoder Fourier Group Harmonics Network for Three-Dimensional Macular Hole Reconstruction with Stochastic Retinal Defect Augmentation and Dynamic Weight Composition

Xingru Huang^{a,d,1}, Yihao Guo^{a,1}, Jian Huang^{a,1}, Zhi Li^{a,*}, Tianyun Zhang^{a,*}, Kunyan Cai^e, Gaopeng Huang^a, Wenhao Chen^a, Zhaoyang Xu^c, Liangqiong Qu^f, Ji Hu^a, Tinyu Wang^a, Shaowei Jiang^a, Chenggang Yan^a, Yaoqi Sun^{h,*}, Xin Ye^{b,*}, Yaqi Wang^{g,*}

^aHangzhou Dianzi University, Hangzhou, China.

^bDepartment of Ophthalmology, Zhejiang Provincial People's Hospital, Hangzhou, China.

^cDepartment of Paediatrics, University of Cambridge, Cambridge, CB2 1TN, UK.

^dSchool of Electronic Engineering and Computer Science, Queen Mary University of London, London, E3 4BL, UK

^eFaculty of Applied Sciences, Macao Polytechnic University, 999078 Macao SAR, China.

^fThe University of Hong Kong, Hong Kong, China.

^gCollege of Media Engineering, Communication University of Zhejiang, China.

^hLishui Institute of Hangzhou Dianzi University, Lishui, China.

ARTICLE INFO

Article history:

Received 1 May 2023

Received in final form 10 May 2023

Accepted 13 May 2023

Available online 15 May 2023

Communicated by S. Sarkar

Keywords:

Fundus retinal segmentation

Macular hole

Macular edema detection

Fundus reconstruction

Ophthalmology

ABSTRACT

The spatial and quantitative parameters of macular holes are vital for diagnosis, surgical choices, and post-op monitoring. Macular hole diagnosis and treatment rely heavily on spatial and quantitative data, yet the scarcity of such data has impeded the progress of deep learning techniques for effective segmentation and real-time 3D reconstruction. To address this challenge, we assembled the world's largest macular hole dataset, Retinal OCT for Macular Hole Enhancement (ROME-3914), and a Comprehensive Archive for Retinal Segmentation (CARS-30k), both expertly annotated. In addition, we developed an innovative 3D segmentation network, the Dual-Encoder FuGH Network (DEFN), which integrates three innovative modules: Fourier Group Harmonics (FuGH), Simplified 3D Spatial Attention (S3DSA) and Harmonic Squeeze-and-Excitation Module (HSE). These three modules synergistically filter noise, reduce computational complexity, emphasize detailed features, and enhance the network's representation ability. We also proposed a novel data augmentation method, Stochastic Retinal Defect Injection (SRDI), and a network optimization strategy DynamicWeightCompose (DWC), to further improve the performance of DEFN. Compared with 13 baselines, our DEFN shows the best performance. We also offer precise 3D retinal reconstruction and quantitative metrics, bringing revolutionary diagnostic and therapeutic decision-making tools for ophthalmologists, and is expected to completely reshape the diagnosis and treatment patterns of difficult-to-treat macular degeneration. The source code is publicly available at: <https://github.com/IIPL-HangzhouDianUniversity/DEFN-Pytorch>.

© 2023 Elsevier B. V. All rights reserved.

1. Introduction

Similar to glaucoma and cataracts, macular degeneration is a leading cause of vision loss and is widely recognized as a challenging eye condition to address (Coleman et al., 2010). The

*Corresponding author:

e-mail: wangyaqi@cuz.edu.cn (Yaqi Wang)

¹These authors have contributed equally to this work.

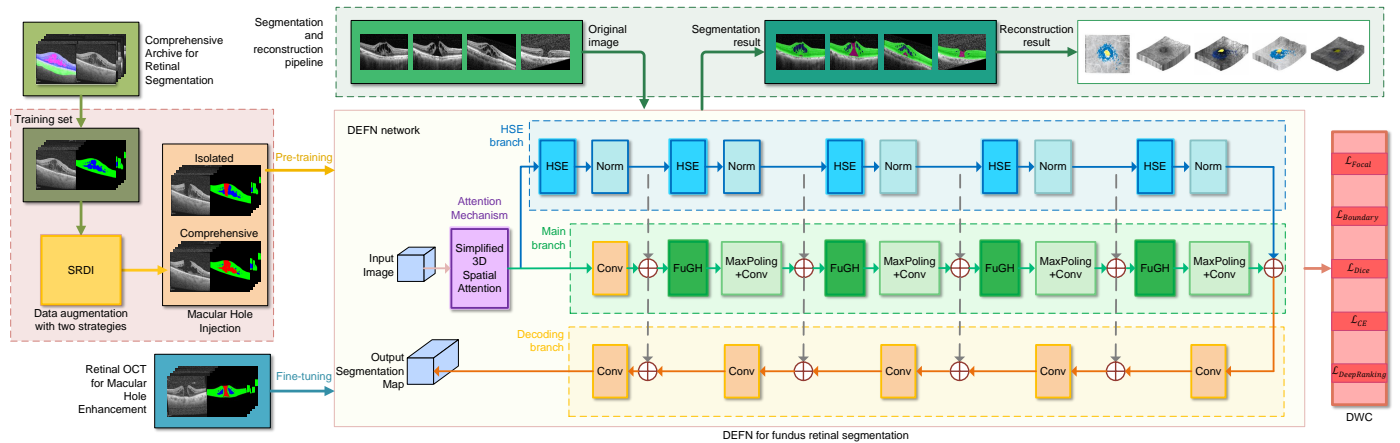


Fig. 1: Schematic representation of the project workflow encompassing a data augmentation pipeline employing SRDI (a data amplification technology), pre-training and fine-tuning phases for the DEFN model, and the segmentation and reconstruction pipelines. SRDI includes two strategies: isolated macular hole injection and comprehensive macular hole injection. The DWC, a dynamic weight fusion network optimization strategy, is integrated within this workflow to enhance the model performance.

tion, and quantitative medication during the treatment process.

To counter these challenges, we’ve proposed a novel macular hole segmentation network, Dual-Encoder FuGH Network (DEFN²). Our DEFN encompasses the Fourier Group Harmonics (FuGH) module, the Simplified 3D Spatial Attention (S3DSA) module, and the Harmonic Squeeze-and-Excitation Module (HSE), designed to enhance the segmentation accuracy and robustness of the macular hole and other critical structures. The FuGH module, through frequency-domain group convolution, improved the recognition of periodic patterns, thereby reducing noise influence and enhancing segmentation accuracy. The S3DSA module, by self-adapting the weight distribution across multiple spatial attention layers, has effectively enhanced the accuracy of identifying hard-to-tag areas like the macular hole and macular edema. HSE module, through learning complex inter-channel weight patterns, precisely emphasized critical features, further boosting the model’s segmentation capacity.

For the development of DEFN, we spent five years assembling the world’s largest dataset on macular holes, Retinal OCT for Macular Hole Enhancement (ROME-3914), and a considerable retinal segmentation dataset, Comprehensive Archive for Retinal Segmentation (CARS-30k), manually annotated by experienced clinicians for the macular hole, macular edema, retina, and ocular fundus retinal structures. We first utilized a novel data expansion technique, Stochastic Retinal Defect Injection (SRDI), to expand the macular hole in the ROME-3914 dataset, pre-trained it on the DEFN, and finally fine-tuned and tested it on the CARS-30k dataset. According to our CARS-30k evaluation, DEFN significantly outperforms traditional models in its ability to segment the macular hole. Moreover, we provided a novel 3D structure reconstruction solution to visualize the ocular fundus retina in three dimensions. Based on the ET-DRS zoning chart, the derived quantitative metrics can provide

guidance for doctors in the diagnosis and treatment of diseases. Our study’s primary contributions are summarized as follows:

1. We collected and annotated the largest macular hole dataset in the world today and a sizable retinal segmentation dataset for auxiliary training.

2. We proposed the SRDI data augmentation method, effectively addressing the shortages in macular hole data and sequence sizes. Simultaneously, it crucially impacts the expansion of other small datasets.

3. We proposed a brand-new DEFN, with three innovative built-in modules, delivering impressive segmentation results on the macular hole and other clinically challenging diseases.

4. We proposed the concept of DynamicWeightCompose (DWC). Any task can fuse suitable loss function according to DWC concept and dynamically adjust the loss function strategy at different training periods.

5. We performed 3D modeling of retinal segmentation results and calculated quantitative indicators to enhance clinical efficiencies in treating various diseases.

More background and related works are exhaustively discussed in Chapter 2. All methods mentioned above are described in detail in Chapter 3. Experimental data is provided in Chapter 4, along with comprehensive evaluation results. In-depth discussions about clinical impacts are provided in Chapter 5. The conclusion is given and concluded in chapter 6.

2. Related work

Segmentation has been a cornerstone in image processing, with advancements spanning various domains. The evolution of segmentation techniques has been significantly influenced by the rise of deep learning, particularly CNNs (Yang *et al.*, 2019). In the realm of 3D segmentation, the transition from traditional methods to deep learning-based approaches has been evident (Niyas *et al.*, 2022). The 3D U-Net, for instance, has emerged as a popular choice for volumetric data segmentation, offering superior performance in various applications (Çiçek *et al.*, 2016).

²The sourcecode is publicly available at: <https://github.com/IIPL-HangzhouDianUniversity/DEFN-Pytorch>.

Medical image segmentation has witnessed remarkable progress with the advent of machine learning techniques. Deep neural networks, in particular, have established new benchmarks in medical image segmentation tasks. In the 3D medical segmentation domain, architectures like 3D U-Net have been pivotal, demonstrating robustness across different datasets (Isensee *et al.*, 2021). Based on 3D U-Net, researchers have proposed a myriad of architectures, including but not limited to V-Net, 3D UX-NET, UNETR, MultiResUNet, Swin UNETR, ResUNet, DeepResUNet, ST U-Net (Milletari *et al.*, 2016; Lee *et al.*, 2022; Hatamizadeh *et al.*, 2022; Ibtehaz and Rahman, 2020; Hatamizadeh *et al.*, 2021; Xu *et al.*, 2019; Zhang *et al.*, 2018; Huang *et al.*, 2023) and others. Of course, there are other network architectures besides the aforementioned, such as nnFormer, SegResNet, TransBTS, HighRes3DNet, SegCaps (Zhou *et al.*, 2021; Myronenko, 2019; Wang *et al.*, 2021; Li *et al.*, 2017; LaLonde and Bagci, 2018) and others. These networks show good performance for different tasks.

In the relentless pursuit of enhanced medical image segmentation, several seminal works have come to the fore. Dai *et al.* have introduced CAN3D, a compact convolutional network tailored for real-time 3D MR image segmentation on clinical workstations with constrained computational resources (Dai *et al.*, 2022). This innovation significantly mitigates computational burdens while preserving a commendable level of accuracy, notably in challenging scenarios with imbalanced classes. Concurrently, Xia *et al.* have directed their focus towards the segmentation of vessel-like structures in 3D medical images, proposing the edge-reinforced neural network to ameliorate the segmentation of crisp edges within these structures, a common challenge attributed to the imbalanced distribution of edge and non-edge voxels (Xia *et al.*, 2022). In a parallel endeavor, Alalwan *et al.* have crafted the 3D-DenseUNet-569 for efficient liver and tumor segmentation, effectively reducing GPU memory requirements and computational costs, showcasing the model's effectiveness and efficiency on a standard LiTS dataset (Alalwan *et al.*, 2021). Lastly, Kamnitsas *et al.* have ventured into the domain of brain lesion segmentation, articulating a dual pathway 3D CNN that demonstrated improved performance on various benchmarks, thus underscoring the potential of deeper 3D CNNs in medical imaging (Kamnitsas *et al.*, 2017). These pioneering endeavors exemplify a notable stride towards more accurate and efficient segmentation methods in medical image analysis, enriching the domain with robust and computationally efficient models poised to tackle a diverse array of segmentation tasks.

The incorporation of novel operators like Fast Fourier Transform (FFT) and wavelet transform in neural networks has shown promising results. FFT, in particular, has been extensively explored for its potential to enhance network performance. The integration of FFT with CNNs (Krizhevsky *et al.*, 2012) has led to improved accuracy and computational efficiency in various tasks (Lin *et al.*, 2018).

The choice of loss function is pivotal in training deep learning models for segmentation tasks. Among them, \mathcal{L}_{Dice} and $\mathcal{L}_{CrossEntropy}$ are widely adopted for their simplicity and efficacy. The \mathcal{L}_{Focal} (Lin *et al.*, 2017), on the other hand, is de-

signed to address the challenge of class imbalance by down-weighting well-classified examples. The $\mathcal{L}_{UnifiedFocal}$ (Yeung *et al.*, 2022) provides a comprehensive framework that encompasses both \mathcal{L}_{Dice} and $\mathcal{L}_{CrossEntropy}$. Furthermore, $\mathcal{L}_{Boundary}$ (Kervadec *et al.*, 2019) emphasizes the importance of accurate boundary detection in segmentation. However, these loss functions often excel in specific areas while falling short of offering comprehensive improvements.

The field of ophthalmology has benefited from the advancements in segmentation techniques. For instance, the segmentation of retinal vasculature has been enhanced by fully convolutional neural networks and novel transfer learning-based approaches (Morano *et al.*, 2020). Lin *et al.* propose a stimulus-guided adaptive transformer network for accurate retinal blood vessel segmentation (Lin *et al.*, 2023). Moreover, methods like the boundary-aware context neural network have been proposed for precise segmentation in ophthalmological images (Wang *et al.*, 2022). Lin *et al.* made significant progress in few-shot semantic segmentation by reformulating images as a semantic reconstruction problem (Liu *et al.*, 2021). They introduced the concept of anti-aliasing semantic reconstruction which provides a systematic solution for few-shot learning problems. Another study by Zhang *et al.* proposed a segment-sliding reconstruction scheme for effectively reconstructing Nyquist samples, which has potential applications in ophthalmology imaging (Zhang *et al.*, 2015). Hu *et al.* proposed a method that combines deep neural networks and atrous spatial pyramid pooling for the automatic segmentation of subretinal fluid and pigment epithelium detachment lesions in OCT images (Hu *et al.*, 2019).

Optical Coherence Tomography (OCT) has become an indispensable tool for diagnosing and monitoring retinal diseases such as the macular hole and the macular edema. He *et al.* proposed a method using deep networks for structured layer surface segmentation in retinal OCT images (He *et al.*, 2021). Guo *et al.* introduced the retinal fluid segmentation network (ReFNet) for segmenting volumetric retinal fluid in OCT volumes, particularly focusing on diabetic macular edema (Guo *et al.*, 2020). Their approach combined both OCT and angiography (OCTA) scans for improved segmentation accuracy. Bai *et al.* presented a method for cystoid macular edema (CME) segmentation in retinal OCT images using a fully convolutional neural network (FCN) combined with fully connected conditional random fields (Bai *et al.*, 2017). This approach showed promise in segmenting fluid and macular edema areas with high adherence to boundaries. Huang *et al.* established a deep learning model that utilizes OCT images to classify high myopia (HM) eyes with myopic traction maculopathy (Huang *et al.*, 2022). Kugelman *et al.* proposed an OCT image enhancement method based on StyleGAN2, integrating cross-localization techniques and semi-supervised learning to address data scarcity and improve performance (Kugelman *et al.*, 2023).

However, the above methods only focused on segmentation research but did not present an automated framework for combined segmentation and reconstruction.

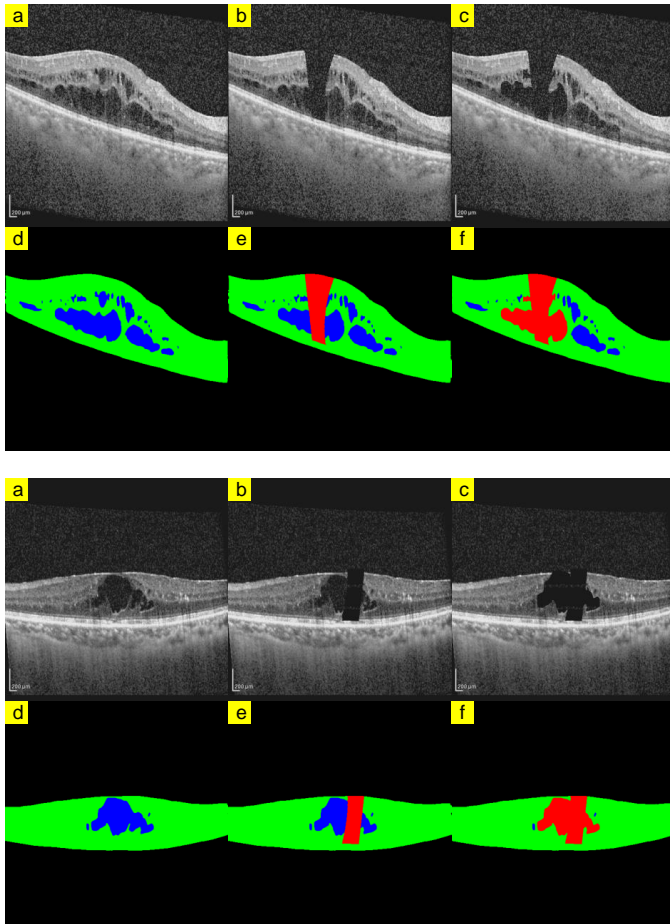


Fig. 2: Results of employing SRDI: (a) original image, (b) image processed with the isolated macular hole injection strategy, (c) image processed with the comprehensive macular hole injection strategy, (d) corresponding mask for (a), (e) corresponding mask for (b), and (f) corresponding mask for (c). Different color in masks represent different eye conditions: the green area represents the retina, the red area represents the macular hole, and the blue area represents the macular edema.

3. Method

In the field of 3D image segmentation of optical coherence tomography (OCT) of the fundus, the retina can be accurately segmented due to its simple structure and prominent features. However, for blurred regions with indistinct boundaries like the macular hole and macular edema that are easily confused with vitreous opacities, there is still no research that can clearly segment the macular hole and macular edema. In addition, datasets related to the macular hole are usually small in sample size, with short single sample sequences, further restricting the improvement of model performance in segmenting the macular hole. Finally, the loss functions used in medical image segmentation often only have good segmentation performance improvement effects on specific regions such as overall or boundaries, with limited improvement in overall segmentation performance and poor transferability to other tasks. To address the aforementioned challenges, we propose the innovative data augmentation method SRDI, the segmentation network DEFN better suited for complex images, and the cutting-edge loss function application method DWC. First, the SRDI

technique addresses the problem of the macular hole sample scarcity by randomly injecting simulated macular hole and sequence expansion to enrich the training set. Second, DEFN integrates three innovative modules: Fourier Group Harmonics (FuGH), Simplified 3D Spatial Attention (S3DSA) and Harmonic Squeeze-and-Excitation Module (HSE), which can effectively solve problems such as noise, blurred labels, and complex structural hierarchies in OCT images, thereby significantly improving the segmentation accuracy and robustness of the macular hole and other key structures. Finally, DWC introduces a dynamic weighting mechanism to fuse multiple loss functions, further improving the model's accuracy in handling difficult-to-segment regions such as the macular hole and the macular edema. The complete architecture is shown in Fig.1, and this section will introduce SRDI, DEFN and DWC in order and discuss their design principles.

3.1. Stochastic Retinal Defect Injection

There are two key challenges for retinal structure reconstruction and data analysis tasks involving the macular hole. Firstly, the boundaries of the macular hole are unclear and difficult to distinguish from intraretinal vitreous opacities and other interfering opacities. Secondly, OCT datasets containing the macular hole tend to have small sample sizes, with each sample comprising a limited number of slices. Even with the largest available macular hole dataset, training AI models to achieve satisfactory macular hole segmentation performance remains challenging.

To address the paucity of macular hole samples for model development and validation, we devised a novel data augmentation technique termed Stochastic Retinal Defect Injection, SRDI. SRDI incorporates two methods: sequence expansion and macular hole injection. Through sequence expansion, samples from an auxiliary retinal segmentation dataset are expanded to an appropriate number of slices. Subsequently, by randomly injecting simulated macular hole into OCT images of the retina with macular edema, the number of macular hole samples is effectively increased. However, randomly injecting simulated macular hole risks obscuring the original macular edema regions, potentially generating overlapping labels for the macular hole and macular edema. To solve this issue, SRDI designed two injection strategies. The first is "isolated macular hole injection", which only creates isolated macular holes within the retinal OCT image without labeling the connected edematous area. The second is "comprehensive macular hole injection", which additionally labels directly connected edematous areas as the macular hole. The effects of the two strategies are shown in Fig.2.

For the isolated macular hole injection strategy, a random twist intensity and voxel center coordinate are first calculated from the expanded 3D voxels. For each slice of the voxel, the primary and secondary radii are calculated based on the y-coordinate, and the region representing the macular hole is annotated based on these radii and center coordinate for each slice, as shown in b and e in Fig.2.

For the comprehensive macular hole injection strategy, in addition to the same steps as isolated strategy, a depth-first search

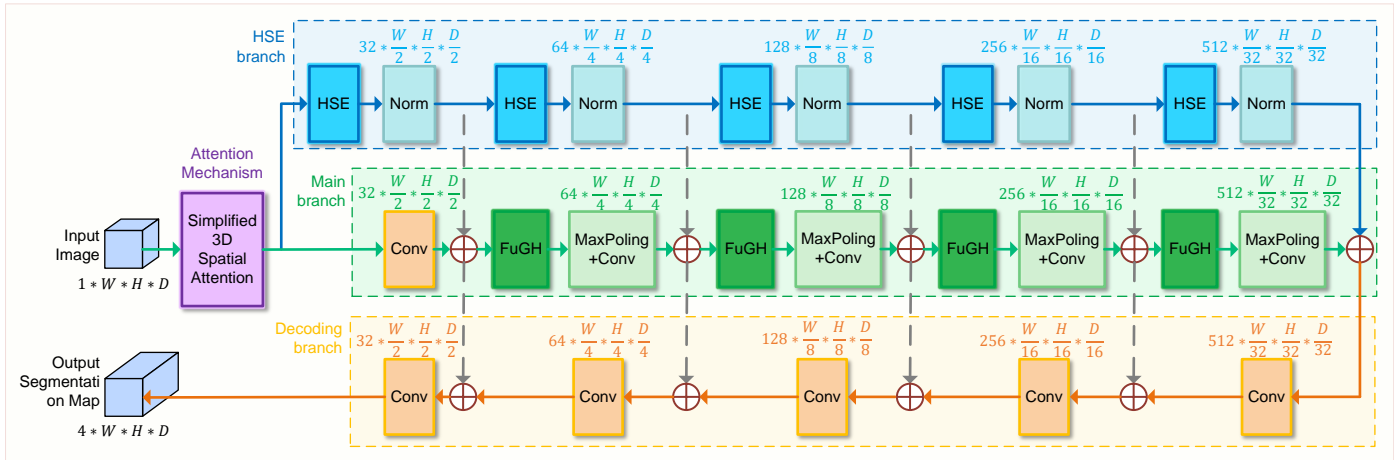


Fig. 3: Schematic representation of the DEFN architecture, encompassing a Main branch, an HSE branch, and a Decoding branch. Within the HSE branch, five consecutive HSE modules are interlaced with Norm modules. The Main branch is structured with a Conv layer, four continuous FuGH modules, a MaxPooling operation, and subsequent Conv layers. The Decoding branch comprises five Conv layers. Integral to this architecture is a Simplified 3D Spatial Attention mechanism, honing the model's focus on relevant spatial features.

algorithm is used to label all edema regions directly connected to the generated macular hole region boundary as macular hole, as shown in c and f in Fig.2.

For both comprehensive and isolated strategies, a 15-pixel isolation boundary is added after generating the macular hole region.

Regardless of whether it is a comprehensive or isolated strategy, the pre-segmentation original image can be generated from the corresponding post-segmentation image in the same way. Mask preprocessing is first performed to identify the macular hole region, and then a specific region is cropped from the background of the original image. After stitching and Gaussian blur processing, this processed region is overlaid onto the original image macular hole region to realistically simulate the actual presence of the macular hole.

3.2. Dual-Encoder Fourier Group Harmonics Network

Segmentation of 3D OCT retinal images requires not only precise localization and labeling of target regions such as the macular hole and the macular edema within complex hierarchical structures but also robustness against environmental noise and other interfering factors. To address these challenges, we propose the Dual-Encoder FuGH Network for 3D segmentation of OCT retinal images. This network employs a primary encoder and an auxiliary encoder, incorporating three key modules: Fourier Group Harmonics (FuGH), Simplified 3D Spatial Attention (S3DSA) and harmonic squeeze-and-excitation (HSE).

The FuGH module aims to address the issue of recognizing periodic and symmetric structures. Compared to conventional CNNs, FuGH improves the recognition of periodic patterns through frequency domain grouped convolutions, thereby reducing noise effects and improving segmentation accuracy. The S3DSA module is designed to address issues of uneven anatomical layers and blurred labels in 3D OCT images. It adaptively adjusts the weights of multi-layer spatial attention distributions to increase the weights of macular hole and macular edema re-

gions, demonstrating higher sensitivity and effectively improving the accuracy of identifying difficult-to-label regions such as the macular hole and the macular edema. The HSE (Harmonic Squeeze-and-Excitation) module enhances dependencies between channels by learning complex inter-channel weighting patterns, accurately highlighting important features and further enhancing the model's discrimination ability.

Overall, these three modules work together to effectively address noise, blurred labels, and hierarchical complexity in 3D OCT retinal image segmentation. Experimental results validate that the integration of these modules enables the DEFN to excel at segmenting the intraretinal macular hole, with the potential applicability to other medical image segmentation tasks. The detailed network structure and module design are shown in Fig.3.

3.2.1. Overall structure

In segmentation tasks, feature extraction is of utmost importance. However, segmenting irregularly distributed macular edema in the retina and predicting the upper boundaries of the macular hole are often complicated by noise interferences in OCT retinal scans, due to factors such as vitreous opacity and environmental disturbances. This noise affects the boundary segmentation of macular edema and upper boundary prediction of the macular hole, thereby making effective feature extraction more challenging. To reduce noise and enhance feature extraction, the network's encoder design includes two channels, as shown in Fig.3. In the primary channel, the FuGH module and CNN downsampling are used, where FuGH processes frequency domain information to reduce noise interference, and CNN extracts deep spatial features. In the auxiliary channel, the model introduces both FuGH and Harmonic Squeeze-and-Excitation (HSE) modules. The FuGH obtains a larger field of view in the frequency domain, followed by the HSE module, which increases the weights of positive feature channels while suppressing various negative feature channels. Finally, the features are inputted to the primary channel and the next level via

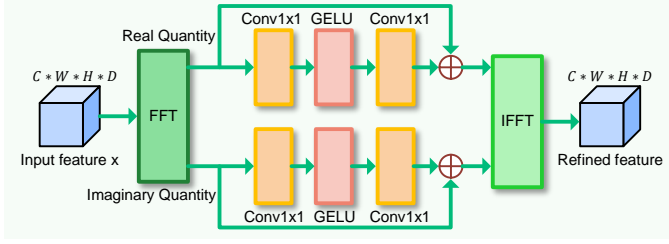


Fig. 4: Schematic representation of the FuGH module, initiating with an FFT operation that segregates the input into real and imaginary components. These components are then sequentially channeled through a Conv layer, a GELU activation function, and a subsequent Conv layer on both upper and lower pathways. Following these processing stages, an IFFT operation is executed to yield the final output.

CNN downsampling. Each downsampling increases the feature channels to twice and reduces the feature dimensions to 1/2 of the original. The decoder of the model combines the output of the previous level with the features from the corresponding position of the encoder, first through ResBlock and upsampling. Correspondingly, each upsampling reduces the feature channels to half and increases the feature dimensions to twice the original. As this involves a multi-class task, after four upsamplings, CNN is used to transform the channels to the number of categories, with each channel representing the segmentation result of each class. The overall network structure is shown in Fig.3.

3.2.2. Fourier Group Harmonics

Noise is often present in OCT images and can negatively impact segmentation results. However, in traditional convolutional neural networks, feature extraction is accomplished through spatial domain convolutions, which are often sensitive to noise, making the model susceptible to noise interference. To address this issue, we propose the Fourier Group Harmonics (FuGH) module. This module uses Fourier transformation to convert the input data from the spatial domain to the frequency domain for feature extraction, enabling model to better understand the frequency characteristics of the data. In the frequency domain, the model can identify and filter out unnecessary high-frequency or low-frequency noise, thereby denoising the data, as shown in the flowchart in Fig.4. FuGH is not simply a Fourier transform of the data. By introducing group-based convolutional operations in the frequency domain, FuGH enables targeted feature extraction and modification within specific frequency ranges. This enhances the model's ability to capture periodic patterns in the data. Meanwhile, the group-based operations also effectively reduce the number of parameters and computational complexity.

Specifically, for input x , we first perform a three-dimensional fast fourier transform (FFT) to obtain its representation in the frequency domain:

$$x_{fft} = FFT(x) \quad (1)$$

Hereafter, we separately process the real and imaginary parts of the data in the frequency domain. For real and imaginary parts, we apply two grouped convolutional operations with a GELU activation function inserted in between, and add a residual connection:

$$y_{fft_{real}} = Conv_2(GELU(Conv_1(x_{fft_{real}}))) + x_{fft_{real}} \quad (2)$$

$$y_{fft_{imag}} = Conv_2(GELU(Conv_1(x_{fft_{imag}}))) + x_{fft_{imag}} \quad (3)$$

Here, $Conv_1$ and $Conv_2$ denote the first and second grouped convolutional operations, respectively. And $x_{fft_{real}}$ and $x_{fft_{imag}}$ denote the real and imaginary parts of the x_{fft} , respectively.

Lastly, we combine the processed real and imaginary parts and perform an inverse fast fourier transform (IFFT) to return the spatial domain representation:

$$y_{out} = IFFT(Complex(y_{fft_{real}}, y_{fft_{imag}})) \quad (4)$$

The FuGH module provides the model with a new dimension to understand and extract key information from the data, especially when dealing with tasks involving clear and complex frequency patterns, such as image processing.

3.2.3. Simplified 3D Spatial Attention

The macular hole are difficult to extract features given their blurred boundaries with the retina and propensity for confusion with vitreous opacities, resulting in often suboptimal segmentation performance. Segmenting the macular hole is a key focus as well as a challenge of this task. Improving the ability to segment the macular hole and the macular edema relies crucially on effective feature extraction.

Various attention mechanisms are commonly used in 3D segmentation. Through experimenting with multiple attention mechanisms, the best overall performance was achieved with spatial attention (Jaderberg et al., 2015), likely because spatial attention focuses on activating specific spatial regions, which is highly effective for addressing vitreous opacities and background noise encountered when segmenting retinal the macular hole. Therefore, we selected spatial attention and further simplified it, yielding the Simplified 3D Spatial Attention (S3DSA) structure shown in Fig.5.

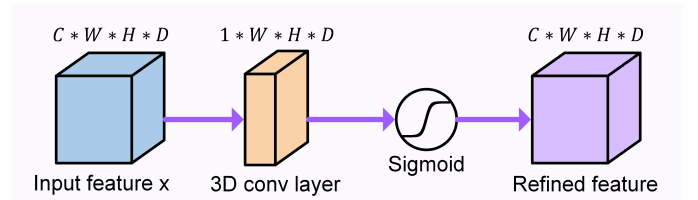


Fig. 5: Schematic representation of the S3DSA module, which initially channels the input through a 3D convolutional layer, followed by a Sigmoid activation function. This configuration facilitates effective feature extraction while maintaining a simplistic structural framework.

S3DSA uses a 3D convolutional layer to process the original input features, generating attention weights, followed by a sigmoid activation function to constrain the attention weights within the range of $[0, 1]$. The sigmoid activation function is:

$$S(x) = \frac{1}{1 + e^{-x}} \quad (5)$$

Finally, the original input features x and the attention weights $Attention_{sigmoid}$ that were normalized by the sigmoid function

undergo an element-wise multiplication to obtain the weighted output. This can be represented by the formula:

$$\text{Output} = x \odot \text{Attention}_{\text{sigmoid}} \quad (6)$$

By preprocessing the input using S3DSA, the network is able to focus attentional resources on more important macular hole and macular edema regions within the input volume. This helps to improve segmentation quality. Furthermore, S3DSA simplifies the underlying spatial attention mechanism through structural simplification steps that remove unnecessary operations, optimizing the design for higher computational efficiency.

3.2.4. Harmonic Squeeze-and-Excitation Module

Compared to the retina, the boundary between the macular hole and the macular edema is not clearly defined, and it is difficult to distinguish macular hole from vitreous opacity and proliferation. Specifically, the upper boundary of the macular hole does not have distinct features, requiring the model to predict the upper boundary using information from a wider field of view, while conventional convolutional kernels have a small field of view and focus more on local information, easily resulting in unclear boundary localization. Therefore, we innovatively proposed the Harmonic Squeeze-and-Excitation Module (HSE), which integrates Fourier Group Harmonics (FuGH) and Squeeze-and-Excitation (SE) blocks with the specific structure shown in Fig.6.

FuGH uses Fourier transforms to convert the image from the spatial domain to the frequency domain to obtain frequency domain information. By performing transformations in the frequency domain, it enables the model to obtain a wider field of view using frequency domain information. Additionally, it filters out unnecessary noise and suppresses unwanted frequency components, such as vitreous opacities, in the frequency domain, enhancing needed frequency components to improve the model's performance. Its formula can be expressed as:

$$y_{FuGH} = FuGH(x) \quad (7)$$

where x and y_{FuGH} are the input and output of FUGH respectively.

The Squeeze-and-Excitation (Hu et al., 2018) block is a dynamic recalibration module that enhances the representational power of the network by adaptively recalibrating channel-wise feature weights. Modeling the importance of each feature channel, helps the model pay attention to those characteristics most meaningful to the current task, and then enhances or suppresses different channels for different tasks. By focusing on those feature channels that distinctly represent the macular hole and macular edema, and suppressing feature channels representing proliferation and vitreous opacity, it improves the model's ability to segment the macular hole and macular edema. Its formula can be expressed as:

$$y_{se} = x \circ \text{Sigmoid}(FC_2(\text{GELU}(FC_1(\text{AvgPool}(x)))))) \quad (8)$$

x is the input of SEBlock, and y_{se} is the output, AvgPool is an adaptive average pooling layer, FC_1 and FC_2 are two fully

connected linear layers, GELU is Gaussian Error Linear Unit. SEBlock can be summarized as follows:

$$y_{se} = SE(x) \quad (9)$$

The HSE module combines FuGH and SE blocks to form a good feature extraction and processing unit, with the model structure shown in Fig.6. For input x , its formula can be expressed as:

$$x_1 = LN(\text{Conv}_1(LN(\text{FuGH}(x)))) \quad (10)$$

$$y_{out} = DP(SE(\text{Conv}_3(\text{GELU}(LN(\text{Conv}_2(x_1))))) + x_1 \quad (11)$$

where y_{out} is the output of HSE module, DP refers to DropPath, a regularization technique used to prevent overfitting. GELU stands for Gaussian Error Linear Unit, which is a specific type of activation function employed to introduce non-linearity in the model. LN is Layer Normalization, a method to normalize the inputs across the features, ensuring smooth training. Conv_i signifies the convolutional function, a cornerstone in convolutional neural networks often used for tasks like image processing.

With this design, we are not only able to capture spatial details but also obtain frequency domain information and suppress interference in the frequency domain, while considering inter-channel correlations to further enhance the representational power of the network. By combining spatial and frequency domain information, the network is able to capture richer and more diverse features, thereby improving the performance of model image segmentation.

3.3. DynamicWeightCompose

A great challenge in segmenting and reconstructing the fundus is precisely segmenting the macular hole and the macular edema from the retinal vitreous opacity and various noises. While many models have good segmentation abilities for the retina itself, it is difficult to achieve satisfactory segmentation effects for the macular hole with less distinct features. A key reason for this is the unreasonable loss function. Specifically, due to the complexity and variability of the retina, it is difficult to correctly locate the target region during segmentation. Therefore, the best-performing loss functions are usually region-based losses, such as cross entropy. However, these region-based loss functions often perform poorly in boundary segmentation, resulting in the inability to accurately annotate the contour of the target region with high precision. On the other hand, although boundary-based losses such as \mathcal{L}_{Focal} or $\mathcal{L}_{Contour}$ may be more precise in boundary segmentation, they often have difficulty accurately locating specific targets such as the macular hole or the macular edema due to the complexity of the internal retinal structure. Therefore, selecting or designing a suitable loss function that considers both regional and boundary information is key to solving this problem.

Existing loss functions often only have good segmentation effects for certain objects, and perform poorly in segmenting features like the macular hole with less prominent features, as well as weak transferability to other tasks. To address this,

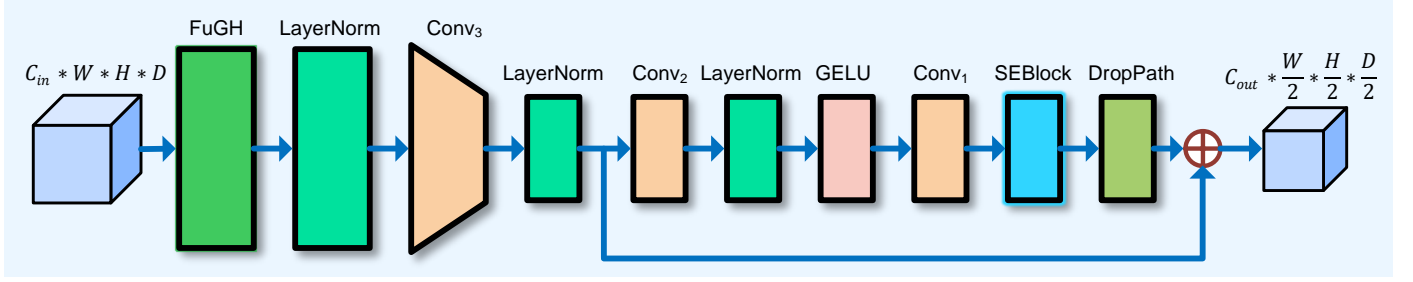


Fig. 6: Schematic representation of the S3DSA module, which initially channels the input through a 3D convolutional layer, followed by a Sigmoid activation function. This configuration facilitates effective feature extraction while maintaining a simplistic structural framework.

we innovatively propose the DynamicWeightCompose (DWC) method. DWC no longer sticks to a particular type of loss, but dynamically fuses losses specialized in different aspects with dynamic weights adjusted according to the training period of the model. In DWC's view, anyone can add or remove losses targeting various difficulties according to their own task needs to create a loss function tailored to their own task. By dynamically adjusting the weights of individual loss functions to match the optimal loss function for each training period, DWC improves model performance.

Based on the concept of DWC, the DynamicWeightCompose Loss (\mathcal{L}_{DWC}) is designed to improve the segmentation of the macular hole in the fundus, while maintaining equally high segmentation performance for the retina and the macular edema. The \mathcal{L}_{DWC} mainly consists of \mathcal{L}_{Focal} , $\mathcal{L}_{Boundary}$, \mathcal{L}_{Dice} , \mathcal{L}_{CE} and $\mathcal{L}_{DeepRanking}$.

\mathcal{L}_{Focal} :

To simultaneously pay attention to the retina, macular edema and macular hole during their segmentation, \mathcal{L}_{Focal} is introduced into the \mathcal{L}_{DWC} . \mathcal{L}_{Focal} is able to concentrate the network's attention on classes with poorer segmentation effects, which greatly improves the segmentation effect of the macular hole.

First, input undergoes a log-softmax transformation to obtain $input_{ls,c}$:

$$input_{ls,c} = \log \left(\frac{e^{input_c}}{\sum_{k=1}^C e^{input_k}} \right) \quad (12)$$

where c is the index number of categories, C is the total number of categories.

Finally, \mathcal{L}_{Focal} is calculated based on $input_{ls,c}$:

$$\mathcal{L}_{Focal} = \frac{1}{N} \sum_{i=1}^N \left[- \left(1 - e^{input_{ls,c}} \right)^Y \times input_{ls,c} \times target \right] \quad (13)$$

where Y is the gamma value, used to reduce the loss of simple samples and enhance the loss of hard-to-classify samples, the target is the result after one-hot encoding of the tensor, N is the total number of voxels, the batch size multiplied by the number of channels multiplied by the spatial size. The integrated loss value uses the mean, making the loss relatively invariant to batch size. This generally results in more stable optimization.

$\mathcal{L}_{Boundary}$:

During macular hole segmentation, the boundary between it and the retina is often blurred, resulting in poor boundary segmentation performance. To emphasize the accuracy of macular hole boundary segmentation, $\mathcal{L}_{Boundary}$ is introduced into the \mathcal{L}_{DWC} .

First, the classification labels are converted to one-hot form through one-hot encoding to more accurately indicate which category each pixel belongs to. Then 3D average pooling is performed to calculate local average values, obtaining the average of all pixel values within a 3D cube of $3 \times 3 \times 3$ centered around each 3D pixel (including the pixel itself).

$$B_{input} = \text{AvgPool3D}(I) - I \quad (14)$$

$$B_{target} = \text{AvgPool3D}(T) - T \quad (15)$$

where I is the input, and T is the target.

Then the mean squared error between the input and target boundaries is calculated through mse_loss to obtain the $\mathcal{L}_{Boundary}$:

$$\mathcal{L}_{Boundary} = \frac{1}{N} \sum_{i=1}^N (B_{input,i} - B_{target,i})^2 \quad (16)$$

\mathcal{L}_{Dice} :

\mathcal{L}_{Dice} is commonly used for image segmentation tasks, especially in medical image segmentation. For fundus segmentation, it has good performance both overall and on boundaries. Therefore, \mathcal{L}_{Dice} is introduced into \mathcal{L}_{DWC} , with the following formula:

$$\mathcal{L}_{Dice} = \frac{1}{N} \sum_{i=1}^N \left(1 - \frac{2 \times I_i + \epsilon_n}{T_i + P_i + \epsilon_d} \right) \quad (17)$$

where I_i is the intersection of the prediction and target for the i^{th} voxel, T_i is the sum of elements in the target for the i^{th} voxel, P_i is the sum of elements in the prediction for the i^{th} voxel, ϵ_n and ϵ_d are smoothing factors.

\mathcal{L}_{CE} :

To enable data preprocessing and compatibility, \mathcal{L}_{CE} is introduced into the \mathcal{L}_{DWC} , with the calculation formula as:

$$\mathcal{L}_{CE} = - \sum_i t_i \log(p_i) \quad (18)$$

where t_i represents the predicted probability that the i^{th} voxel belongs to a certain class, p_i represents the actual label for the i^{th} voxel.

$\mathcal{L}_{DeepRanking}$:

To further improve the segmentation performance of the model, $\mathcal{L}_{DeepRanking}$ is introduced into the \mathcal{L}_{DWC} . $\mathcal{L}_{DeepRanking}$ can distinguish the distance between positive and negative samples, which helps the network perform better in distinguishing positive and negative samples, making positive samples closer to their mean while negative samples further away from their mean, further improving the performance of the model, with the following formula:

$$\mathcal{L}_{DeepRanking} = \max \left(0, m + \sum_{i=1}^N (pos_i - \mu_{pos})^2 - \sum_{j=1}^M (neg_j - \mu_{neg})^2 \right) \quad (19)$$

where N and M are the numbers of positive and negative samples respectively, m is a predefined constant known as the margin, it establishes the minimum gap that should exist between the positive and negative samples in the feature space. pos_i represents the value of the i^{th} positive sample in the feature space, neg_j represents the value of the j^{th} negative sample in the feature space. μ_{pos} and μ_{neg} are the means of positive and negative samples respectively.

The \mathcal{L}_{DWC} integrates the above 5 loss functions and timely adjusts the weights of \mathcal{L}_{Focal} , $\mathcal{L}_{Boundary}$, \mathcal{L}_{Dice} , and \mathcal{L}_{CE} during different training periods, and performs deep ranking on the weighted *total_loss*, achieving a significant improvement in macular hole segmentation performance, with the weighted calculation formula:

$$\mathcal{L}_{Total} = \lambda_{Focal} \times \mathcal{L}_{Focal} + \lambda_{Boundary} \times \mathcal{L}_{Boundary} + \lambda_{Dice} \times \mathcal{L}_{Dice} + \lambda_{CE} \times \mathcal{L}_{CE} \quad (20)$$

where λ_{Focal} , $\lambda_{Boundary}$, λ_{Dice} , λ_{CE} represent the weight of \mathcal{L}_{Focal} , $\mathcal{L}_{Boundary}$, \mathcal{L}_{Dice} , \mathcal{L}_{CE} respectively.

The effectiveness of the DWC method has been validated in the 3D segmentation task of retinal fundus. It can be foreseen that DWC can also provide help to researchers in various tasks in other fields.

4. Experiments and results

In this section, we present the experiment results with quantitative and qualitative evaluations. The influences of different method selections and setups are analyzed.

4.1. Datasets

The DEFN used two datasets for training and evaluation: Retinal OCT for macular hole enhancement (ROME-3914) and Comprehensive archive for retinal segmentation (CARS-30k). A portion of ROME-3914 was selected as the test set, while the remaining part, together with the data augmented using SRDI technology from CARS-30k, served as the training and validation sets. The details of these two datasets will be discussed further below.

4.1.1. Retinal OCT for macular hole enhancement

Over a span of 5 years, we gathered retinal OCT scan data from all patients diagnosed with the macular hole who visited Zhejiang Provincial People's Hospital. We then created a retinal OCT dataset for macular hole enhancement, named ROME-3914. This dataset consists of a total of 3,914 B-scan SD-OCT images (from the Spectralis HRA, Heidelberg Engineering, Germany) containing macular holes. The volume of data and the effort put into data collection surpasses the scale of existing datasets based on public information. Additionally, the annotation quality and precision have reached a new benchmark. The data was collected from patients visiting the Ophthalmology Center of Zhejiang Provincial People's Hospital between May 1, 2016, and December 31, 2021, specifically from those diagnosed with the macular hole. The clinical diagnosis of the macular hole was conducted by a retinal specialist, based on fundus examination, OCT, and angiography. OCT scans exhibiting significant artifacts or those where the signal intensity was reduced to such an extent that retinal interfaces became unidentifiable were excluded. Ultimately, we accumulated OCT scans from 119 macular hole patients, totaling 126 sequences, each sequence consisting of 17 to 115 slices. The OCT volume scans, centered on the macula, covered an area of 6.0×4.5 mm (20°×15°) and had a resolution of 496×512 pixels. The average axial, lateral, and azimuthal pixel spacings were 3.87 micrometers, 11.50 micrometers, and 120.96 micrometers respectively.

A total of 3,914 scanned images from the same device were manually annotated by 5 experienced radiologists between June and December 2021, using segmentation editor software. They marked the retina, the macular edema, and the macular hole in each individual B-scan SD-OCT image. All five doctors annotated each scan, and then two senior retinal experts adjudicated the segmentation results. Throughout this adjudication process, there were multiple rounds of feedback and revisions.

4.1.2. Comprehensive archive for retinal segmentation

In order to supplement the ROME-3914 dataset using SRDI technology, we spent 5 years collecting the retinal OCT scan data of all DME (Diabetic Macular Edema) patients without macular hole who visited the Zhejiang Provincial People's Hospital. We created a comprehensive archive for retinal segmentation as an auxiliary dataset, named CARS-30k. This dataset consists of and annotates a total of 30,684 B-scan SD-OCT images containing macular edema (from the Spectralis HRA, Heidelberg Engineering, Germany). In terms of volume and data quantity, this surpasses all existing efforts based on publicly available information. The data was selected from patients without the macular hole who visited the Ophthalmology Center of Zhejiang Provincial People's Hospital between 2016 and 2021. These patients were diagnosed with DME and underwent anti-VEGF treatment. A retinal specialist made the clinical diagnosis of DME based on fundus examination, OCT, and angiography results. OCT scan data containing severe artifacts or significantly reduced signal strength to the point where the retinal interface could not be identified were excluded. Ultimately, we collected retinal OCT scans from 137 DME patients. The

entire dataset contains 1,476 independent scan sequences, each sequence comprising between 13 to 49 slices, with a resolution of 496x512 pixels each.

Following the same annotation procedure as the ROME-3914 dataset, all images in CARS-30k were manually annotated by 5 radiologists with expertise. After annotation, two senior retinal specialists reviewed and confirmed the annotation results to ensure accuracy and consistency.

The specific information of ROME-3914 and CARS-30k is shown in Table.1.

Table 1: Detailed information of ROME-3914 and CARS-30k, including patient number, sequences number, slices number and resolution.

Dataset name	ROME-3914	CARS-30k
Patients number	119	137
Sequences number	126	1476
Slices number	3914	30684
Resolution	496x512	496x512

4.2. Evaluation metrics

For the two datasets, several evaluation criteria are used: Mean intersection over union (mIOU), Dice coefficient (Dice), Average symmetric surface distance (ASSD), Hausdorff distance (HD), 95th percentile hausdorff distance (HD95), and Adjusted rand index (AdjRand). Among them, mIOU and Dice are region-based measurement methods; ASSD, HD, and HD95 are distance-based measurement methods; while AdjRand is a method based on segmentation consistency. The measurement results for mIOU, Dice, and ASSD are expressed as percentages, whereas those for HD and HD95 are indicated in pixel distances.

Mean intersection over union (mIOU) is an important metric for evaluating the performance of image segmentation tasks, especially in the field of semantic segmentation. It measures the overlap between the predicted segmentation regions and the true segmentation regions.

$$mIOU = \frac{1}{N} \sum_{i=1}^N \frac{|V_{pred,i} \cap V_{true,i}|}{|V_{pred,i} \cup V_{true,i}|} \times 100\% \quad (21)$$

where N is the total number of categories, $V_{pred,i}$ is the region of the i^{th} predicted class, and $V_{true,i}$ is the region of the i^{th} true class.

Dice coefficient (Dice), also referred to as dice similarity coefficient (DSC), is a metric used to measure the similarity between two samples. In image segmentation, it is commonly used to evaluate the overlap between predicted and true regions.

$$Dice = \frac{1}{N} \sum_{i=1}^N \frac{2 \times |V_{pred,i} \cap V_{true,i}|}{|V_{pred,i}| + |V_{true,i}|} \times 100\% \quad (22)$$

Average symmetric surface distance (ASSD), is a commonly used metric for evaluating image segmentation. It measures the

average distance between two surfaces (e.g. the true boundary and predicted boundary). The calculation method is to first calculate the shortest distance from each point to the other surface, and then take the average of all points.

$$ASSD = \frac{1}{N} \sum_{i=1}^N \left(\frac{1}{|S_{true,i}|} \sum_{s \in S_{true,i}} \text{dist}(s, S_{pred,i}) + \frac{1}{|S_{pred,i}|} \sum_{s \in S_{pred,i}} \text{dist}(s, S_{true,i}) \right) \quad (23)$$

where $S_{true,i}$ and $S_{pred,i}$ are the true and predicted voxel sets of the i^{th} surface, respectively. $\text{dist}(s, S)$ represents the minimum distance from voxel s to the surface S . $|S_{true,i}|$ and $|S_{pred,i}|$ are the total number of voxels in the true and predicted voxel sets of the i^{th} surface, respectively.

Hausdorff distance (HD) is a metric that measures the distance between two point sets. In image segmentation, it represents the maximum shortest distance between the predicted and true boundaries.

$$HD = \frac{1}{N} \sum_{i=1}^N \max_{a \in S_{true,i}} \left(\min_{b \in S_{pred,i}} \text{dist}(a, b) \right) \quad (24)$$

where $\text{dist}(a, b)$ is the distance between voxel a in $S_{true,i}$ and voxel b in $S_{pred,i}$.

95th percentile hausdorff distance (HD95) is a variant of hausdorff distance. It does not directly use the maximum distance between all point pairs but takes the 95th percentile of all point pair distances as the result. This can help eliminate outliers caused by extreme values, which may exist in some cases due to noise or segmentation errors.

$$HD95 = \frac{1}{N} \sum_{i=1}^N 95thpercentile \left(\max_{a \in S_{true,i}} \left(\min_{b \in S_{pred,i}} \text{dist}(a, b) \right) \right) \quad (25)$$

where the parameters are consistent with those in the HD formula. The term "95th percentile" refers to the value at the 95th percentile among all the $\max_{a \in S_{true,i}} \left(\min_{b \in S_{pred,i}} \text{dist}(a, b) \right)$ values.

Adjusted rand index(AdjRand) is used to measure the similarity between two data partitions (such as clusters), with the following formula:

$$AdjRand = \frac{\sum_{ij} \binom{n_{ij}}{2} - \left[\sum_i \binom{a_i}{2} \times \sum_j \binom{b_j}{2} \right] / \binom{n}{2}}{\frac{1}{2} \left[\sum_i \binom{a_i}{2} + \sum_j \binom{b_j}{2} \right] - \left[\sum_i \binom{a_i}{2} \times \sum_j \binom{b_j}{2} \right] / \binom{n}{2}} \quad (26)$$

where n_{ij} is the number of data points that are shared between the i^{th} predicted cluster and the j^{th} true cluster. a_i is the number of data points in the predicted cluster i . b_j is the number of data points in the true cluster j . n is the total number of data points. $\binom{n}{2}$ calculates the combinations of choosing 2 from n .

The Adjusted rand index ranges from [-1, 1], where 1 indicates that the two partitions are identical, 0 indicates that the similarity between the two partitions is the same as random partitioning, and -1 indicates that the two partitions are completely inconsistent.

Table 2: Segmentation results employing the isolated macular hole injection method, comparing the proposed DEFN, DEFN+ \mathcal{L}_{DWC} and prior segmentation models. The evaluation spans four classes: All (Average across all classes), MH (Macular Hole), ME (Macular Edema) and RA (Retina). The best values for each metric are highlighted in red, while the second-best values are highlighted in blue, and the values of our model are bolded.

	All					
	mIOU	Dice	ASSD	HD	HD95	AdjRand
3D UX-Net (Lee et al., 2022)	60.40±0.92	68.75±1.11	15.58±352.18	118.17±1783.73	42.08±902.20	68.11±1.10
nnFormer (Zhou et al., 2021)	54.91±0.75	62.85±1.18	19.18±407.92	129.05±1289.18	40.56±778.45	62.13±1.16
3D U-Net (Çiçek et al., 2016)	57.53±0.91	65.51±1.25	14.63±185.15	136.01±2062.75	41.15±1038.55	64.83±1.26
SegResNet (Myronenko, 2019)	60.81±0.75	70.07±0.89	9.79±107.62	181.43±1950.83	37.65±926.18	69.40±0.91
Swin UNETR (Hatamizadeh et al., 2021)	53.98±0.69	60.60±0.85	32.83±755.46	161.96±1993.11	56.15±2464.26	59.67±0.90
TransBTS (Wang et al., 2021)	59.14±0.84	68.88±1.09	12.22±122.52	201.08±2281.63	52.70±2101.74	68.03±1.09
UNETR (Hatamizadeh et al., 2022)	58.31±0.86	67.43±1.13	16.56±228.71	186.03±3462.20	56.02±1386.22	66.72±1.14
DeepResUNet (Zhang et al., 2018)	47.79±0.71	59.94±0.92	32.74±137.32	257.47±690.23	154.22±1461.46	56.72±1.01
ResUNet (Xu et al., 2019)	54.00±0.91	61.72±1.12	26.81±486.61	241.77±4171.18	73.93±4154.42	60.84±1.13
HighRes3DNet (Li et al., 2017)	51.09±1.08	62.30±1.45	25.95±207.02	238.27±1682.30	139.24±3535.07	60.67±1.48
MultiResUNet (Ibtehaz and Rahman, 2020)	53.65±0.99	64.58±1.25	20.94±175.14	234.40±930.15	106.49±3616.22	63.27±1.28
SegCaps (LaLonde and Bagci, 2018)	59.70±0.94	69.14±1.14	8.83±157.57	139.50±4777.57	31.36±2248.22	68.45±1.13
V-Net (Milletari et al., 2016)	60.98±1.11	70.66±1.33	14.88±176.12	188.10±2754.84	56.10±1533.28	69.98±1.35
DEFN	66.09±1.05	75.65±1.16	12.79±150.07	215.05±2771.75	61.01±1691.84	74.97±1.17
DEFN+\mathcal{L}_{DWC}	67.39±1.25	76.71±1.23	5.24±115.48	86.44±1782.33	16.53±417.02	76.06±1.23
	MH					
	mIOU	Dice	ASSD	HD	HD95	AdjRand
3D UX-Net	22.33±4.53	32.34±7.06	44.82±3200.25	219.91±3180.82	116.59±8457.34	32.16±7.02
nnFormer	13.21±2.43	20.59±4.80	54.82±3728.67	213.61±3160.99	108.67±7170.14	20.42±4.75
3D U-Net	15.32±2.38	24.13±4.37	41.59±1628.77	227.28±4386.96	113.46±8643.14	23.97±4.35
SegResNet	24.91±2.79	37.46±4.48	27.03±976.91	225.05±5257.13	101.92±7594.49	37.27±4.45
Swin UNETR	5.79±1.07	9.86±2.36	92.92±6850.08	229.15±4180.83	122.28±10483.45	9.75±2.32
TransBTS	26.08±2.94	38.67±4.76	32.98±1094.25	276.90±5246.63	135.91±13261.41	38.45±4.73
UNETR	22.76±3.09	34.01±5.34	45.06±1979.91	229.00±5851.30	139.85±9085.98	33.78±5.30
DeepResUNet	19.53±1.59	30.98±3.11	66.01±715.13	304.97±904.76	263.75±3878.39	30.49±3.03
ResUNet	10.62±1.74	17.23±3.60	69.58±3789.76	286.78±4977.61	150.52±10854.57	17.04±3.57
HighRes3DNet	27.01±2.62	40.13±4.16	48.70±1168.67	280.35±3045.54	187.99±12353.49	39.84±4.14
MultiResUNet	26.17±2.17	39.64±3.39	40.13±933.65	249.14±916.62	155.12±8972.88	39.38±3.37
SegCaps	28.39±4.29	40.55±6.26	21.91±1291.43	169.68±8233.27	69.87±7775.14	40.32±6.21
V-Net	31.12±3.94	44.07±5.89	40.53±1459.59	183.92±8138.41	146.02±9870.52	43.82±5.89
DEFN	41.35±4.69	54.96±6.44	33.30±1248.53	269.69±3467.38	152.73±9324.47	54.69±6.42
DEFN+\mathcal{L}_{DWC}	42.41±5.79	55.58±6.99	13.91±1054.65	150.27±8648.23	40.62±3715.57	55.38±6.97
	ME					
	mIOU	Dice	ASSD	HD	HD95	AdjRand
3D UX-Net	63.08±3.10	76.08±2.82	1.46±10.17	93.24±4297.60	8.18±360.91	75.74±2.80
nnFormer	56.12±3.24	70.33±3.90	2.11±27.57	118.71±3286.22	10.93±570.85	69.90±3.85
3D U-Net	61.84±3.71	74.75±4.10	1.75±22.90	104.26±4161.35	8.49±403.73	74.39±4.07
SegResNet	61.94±3.38	75.03±3.54	1.78±15.85	119.71±7623.58	9.57±563.32	74.68±3.51
Swin UNETR	62.38±3.39	75.41±3.71	3.00±30.86	137.25±4883.14	25.72±4516.63	75.06±3.67
TransBTS	57.15±3.59	70.98±4.31	2.75±30.15	126.81±6692.50	20.35±3974.09	70.56±4.26
UNETR	56.60±3.49	70.56±4.17	3.95±38.22	148.37±3660.49	24.33±1763.95	70.15±4.13
DeepResUNet	46.43±2.60	61.87±3.45	8.31±110.28	215.54±3168.33	46.65±4189.08	61.43±3.41
ResUNet	57.65±4.00	71.21±4.10	6.74±203.17	205.34±13892.93	43.28±6145.76	70.81±4.08
HighRes3DNet	38.08±2.95	53.06±4.24	13.50±105.16	183.46±4828.31	103.30±3083.48	52.44±4.17
MultiResUNet	43.98±3.24	59.02±4.33	11.96±122.89	202.39±3949.86	92.49±4785.98	58.47±4.29
SegCaps	55.03±3.76	69.08±4.57	3.61±95.44	118.15±5220.89	18.41±4827.90	68.70±4.52
V-Net	55.87±3.39	69.98±3.93	3.48±30.22	164.20±4092.84	20.73±1423.01	69.56±3.89
DEFN	61.16±3.79	74.16±4.33	4.09±43.64	183.25±8426.11	25.50±2656.23	73.82±4.30
DEFN+\mathcal{L}_{DWC}	64.06±3.18	76.75±2.93	1.43±11.17	88.34±3583.72	7.56±437.37	76.44±2.91
	RA					
	mIOU	Dice	ASSD	HD	HD95	AdjRand
3D UX-Net	95.78±0.03	97.84±0.01	0.46±0.40	41.38±2685.38	1.46±1.71	96.43±0.02
nnFormer	95.38±0.05	97.63±0.02	0.62±1.51	54.84±4867.64	2.09±12.36	96.08±0.05
3D U-Net	95.42±0.04	97.65±0.01	0.55±0.54	76.49±5225.30	1.51±1.68	96.12±0.03
SegResNet	95.57±0.03	97.73±0.01	0.57±0.78	199.54±2308.50	1.47±1.74	96.26±0.03
Swin UNETR	93.75±1.18	96.54±0.52	2.57±34.41	119.48±6901.25	20.46±1686.38	94.19±1.55
TransBTS	94.18±0.02	97.00±0.01	0.94±2.31	199.55±3302.21	1.83±1.05	95.08±0.02
UNETR	95.56±0.03	97.73±0.01	0.67±1.93	180.73±6250.51	3.87±236.44	96.24±0.02
DeepResUNet	77.42±0.97	86.98±0.44	23.90±93.95	251.89±405.21	152.28±1667.98	78.24±1.26
ResUNet	93.73±0.12	96.74±0.04	4.13±33.61	233.19±1250.02	27.98±2584.30	94.66±0.09
HighRes3DNet	88.18±0.08	93.70±0.03	15.64±61.53	251.01±313.74	126.44±3959.54	89.73±0.07
MultiResUNet	90.78±0.43	95.08±0.16	10.71±58.95	251.68±323.85	71.86±4538.79	91.96±0.40
SegCaps	95.68±0.03	97.79±0.01	0.96±6.04	130.66±9500.91	5.82±673.51	96.33±0.03
V-Net	95.95±0.03	97.93±0.01	0.63±0.61	216.18±3131.49	1.55±1.09	96.55±0.03
DEFN	95.77±0.03	97.83±0.01	0.98±3.82	192.21±5205.34	4.82±472.13	96.41±0.02
DEFN+\mathcal{L}_{DWC}	95.70±0.02	97.80±0.00	0.38±0.16	20.71±1578.24	1.43±0.68	96.37±0.02

Table 3: Segmentation results employing the comprehensive macular hole injection method, comparing the proposed DEFN, DEFN+ \mathcal{L}_{DWC} and prior segmentation models. The evaluation spans four classes: All (Average across all classes), MH (Macular Hole), ME (Macular Edema) and RA (Retina). The best values for each metric are highlighted in red, while the second-best values are highlighted in blue, and the values of our model are bolded.

	All					
	mIOU	Dice	ASSD	HD	HD95	AdjRand
3D UX-Net	66.28±0.55	77.05±0.52	5.01±18.29	133.14±1525.37	31.54±888.64	76.36±0.52
nnFormer	61.23±0.50	72.49±0.58	4.95±20.81	128.16±1608.05	30.30±1174.56	71.74±0.57
3D U-Net	65.19±0.76	76.00±0.72	6.05±25.77	145.94±2197.05	32.76±1109.64	75.26±0.74
SegResNet	65.10±0.58	76.17±0.61	5.43±22.42	154.90±2464.47	33.37±1073.18	75.42±0.61
Swin UNETR	66.78±0.54	77.48±0.56	6.39±17.92	140.01±1425.83	48.59±880.79	76.80±0.55
TransBTS	60.05±0.48	71.32±0.53	7.92±42.32	194.74±2143.73	46.42±1519.22	70.58±0.53
UNETR	55.51±0.76	66.23±0.96	10.25±61.53	242.12±4507.08	60.09±1611.33	65.44±0.97
DeepResUNet	62.20±0.60	73.16±0.66	10.09±63.23	187.23±2336.72	59.70±1865.69	72.40±0.66
ResUNet	65.20±0.66	75.89±0.68	8.89±52.34	168.65±1990.75	54.77±1703.05	75.15±0.68
HighRes3DNet	51.96±0.62	63.56±0.81	17.30±84.68	210.92±916.36	105.86±2006.60	62.09±0.81
MultiResUNet	63.56±0.83	73.58±0.96	6.20±34.87	198.30±1924.25	24.42±643.94	72.91±0.96
SegCaps	61.01±0.62	72.06±0.62	3.05±4.62	89.24±1751.01	12.60±52.15	71.37±0.62
V-Net	57.42±0.54	68.68±0.64	7.71±43.11	194.97±1815.33	49.10±1237.26	67.86±0.65
DEFN	68.61±0.45	78.84±0.40	3.97±9.27	134.67±2415.95	18.96±445.41	78.18±0.41
DEFN+\mathcal{L}_{DWC}	71.28±0.88	80.92±0.82	2.07±6.64	63.15±1329.20	10.90±318.79	80.28±0.85
	MH					
	mIOU	Dice	ASSD	HD	HD95	AdjRand
3D UX-Net	47.82±1.84	63.61±1.65	11.30±142.62	195.26±4814.95	74.41±6735.95	63.33±1.65
nnFormer	40.09±1.66	56.12±1.91	11.74±126.62	201.63±3857.96	75.89±6560.29	55.80±1.90
3D U-Net	44.04±2.57	59.57±2.77	15.50±202.62	189.67±4974.48	87.62±7889.31	59.25±2.76
SegResNet	47.10±1.89	62.99±1.69	12.78±158.76	199.72±4951.14	84.23±7124.78	62.70±1.69
Swin UNETR	47.83±1.63	63.78±1.53	16.91±145.63	222.46±1759.61	136.84±7367.86	63.48±1.51
TransBTS	39.51±2.10	55.19±2.45	18.95±287.08	213.09±7182.04	116.20±8785.65	54.82±2.44
UNETR	33.63±2.64	48.33±3.46	24.50±398.71	275.86±3619.89	144.84±7867.75	47.90±3.43
DeepResUNet	39.68±2.48	55.26±3.05	24.50±428.03	264.53±7214.70	142.12±8690.23	54.92±3.05
ResUNet	46.66±2.86	61.98±3.17	20.63±343.31	226.39±3096.04	124.63±8732.36	61.69±3.16
HighRes3DNet	33.54±2.48	48.30±3.52	31.30±398.49	235.48±968.94	175.98±5385.78	47.83±3.50
MultiResUNet	32.63±2.06	47.70±2.82	15.60±301.28	224.51±2047.13	58.36±5659.28	47.45±2.81
SegCaps	38.85±1.89	54.70±2.11	7.36±36.73	163.98±5913.54	30.70±433.96	54.40±2.10
V-Net	37.53±2.39	52.88±3.00	18.21±276.97	221.46±5140.60	127.90±7791.50	52.50±2.98
DEFN	43.75±1.60	59.86±1.74	10.01±80.50	208.59±3954.24	46.54±3930.02	59.58±1.74
DEFN+\mathcal{L}_{DWC}	50.72±3.31	65.42±3.78	4.90±58.23	96.72±6482.97	26.27±2908.25	65.21±3.78
	ME					
	mIOU	Dice	ASSD	HD	HD95	AdjRand
3D UX-Net	55.24±2.96	69.72±3.48	3.02±29.62	146.42±2975.81	14.52±998.73	69.34±3.44
nnFormer	48.12±2.52	63.67±2.94	2.47±25.26	132.23±2891.56	12.08±1104.20	63.24±2.89
3D U-Net	56.09±2.25	70.76±2.07	2.02±18.66	129.57±3428.75	9.18±946.98	70.38±2.08
SegResNet	52.82±2.46	67.89±3.14	3.01±27.55	140.12±2844.75	14.38±1196.73	67.50±3.12
Swin UNETR	56.61±3.21	70.74±3.70	1.78±19.53	115.40±3617.85	7.64±430.40	70.38±3.66
TransBTS	44.83±1.70	60.91±2.27	3.50±47.66	149.72±4156.99	15.79±1945.61	60.48±2.25
UNETR	37.41±2.41	52.67±3.61	5.22±47.65	237.52±8483.70	31.52±2533.88	52.24±3.61
DeepResUNet	51.50±2.66	66.57±3.48	4.41±42.30	156.06±4054.38	26.25±2159.98	66.15±3.46
ResUNet	53.53±3.22	68.05±3.99	4.51±55.09	150.63±3337.24	18.75±2660.96	67.64±3.95
HighRes3DNet	32.43±1.69	47.74±2.70	9.67±56.05	153.37±3013.19	64.10±3035.82	47.18±2.65
MultiResUNet	62.34±3.58	75.25±4.01	1.97±25.56	149.94±3771.84	8.50±381.78	74.90±3.98
SegCaps	48.45±2.93	63.68±2.98	1.36±7.07	56.19±2409.45	5.57±117.26	63.33±2.93
V-Net	39.63±1.61	55.68±2.22	3.63±50.35	137.23±2658.35	16.22±1713.99	55.28±2.21
DEFN	66.26±2.42	78.79±2.08	1.26±10.83	111.26±4613.60	5.63±278.02	78.49±2.08
DEFN+\mathcal{L}_{DWC}	67.32±2.64	79.48±2.21	0.91±2.49	66.30±3180.87	4.98±130.41	79.20±2.20
	RA					
	mIOU	Dice	ASSD	HD	HD95	AdjRand
3D UX-Net	95.76±0.02	97.83±0.01	0.71±2.91	57.74±4268.90	5.69±408.12	96.42±0.02
nnFormer	95.49±0.03	97.69±0.01	0.63±1.66	50.61±5406.32	2.93±96.93	96.18±0.03
3D U-Net	95.44±0.03	97.66±0.01	0.63±1.37	118.58±7731.80	1.47±0.46	96.47±0.02
SegResNet	95.38±0.04	97.63±0.01	0.49±0.29	124.85±6449.70	1.51±1.09	96.06±0.04
Swin UNETR	95.91±0.02	97.91±0.01	0.47±0.63	82.18±6040.85	1.29±0.58	96.55±0.02
TransBTS	95.82±0.04	97.86±0.01	1.33±9.62	221.42±1406.87	7.25±946.92	96.43±0.04
UNETR	95.48±0.03	97.68±0.01	1.03±1.73	212.99±3753.99	3.89±106.82	96.16±0.03
DeepResUNet	95.43±0.03	97.65±0.01	1.37±7.80	141.10±6939.90	10.72±1466.80	96.12±0.03
ResUNet	95.41±0.05	97.64±0.01	1.53±10.43	128.92±6166.71	10.92±1292.76	96.11±0.04
HighRes3DNet	89.90±0.17	94.64±0.06	10.93±49.03	243.92±476.21	77.49±5093.44	91.26±0.14
MultiResUNet	95.71±0.04	97.80±0.01	1.02±8.06	220.45±3934.93	6.41±730.20	96.37±0.03
SegCaps	95.74±0.03	97.82±0.01	0.43±0.26	47.54±4506.35	1.54±2.33	96.38±0.03
V-Net	95.08±0.05	97.47±0.01	1.28±1.83	226.23±1373.02	3.20±119.15	95.80±0.05
DEFN	95.83±0.03	97.86±0.01	0.64±3.87	84.15±8430.80	4.70±496.22	96.47±0.02
DEFN+\mathcal{L}_{DWC}	95.80±0.02	97.85±0.01	0.41±0.37	26.44±2294.00	1.43±0.82	96.44±0.02

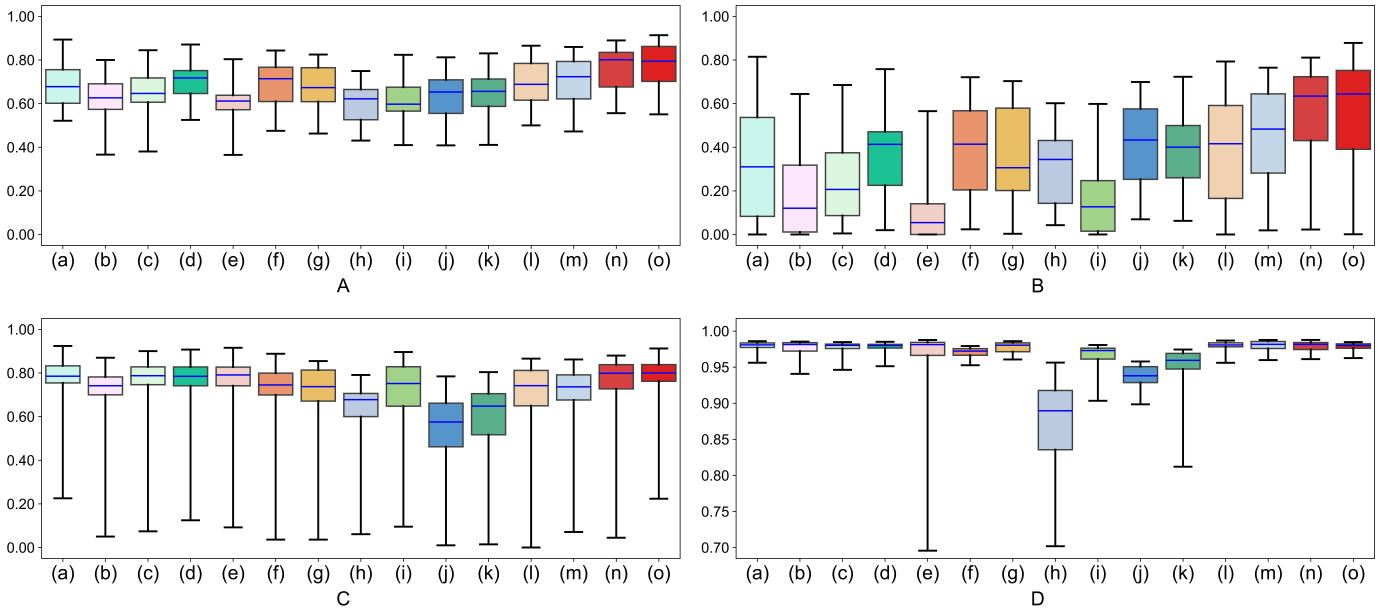


Fig. 7: Box plot showcasing the Dice index from training results using the isolated macular hole injection method. The categories are represented as: table A (Average across all classes), table B (Macular Hole), table C (Macular Edema) and table D (Retina). On the x-axis, the models are labeled as: (a) 3D UX-Net; (b) nnFormer; (c) 3D U-Net; (d) SegResNet; (e) Swin UNETR; (f) TransBTS; (g) UNETR; (h) DeepResUNet; (i) ResUNet; (j) HighRes3DNet; (k) MultiResUNet; (l) SegCaps; (m) V-Net; (n) DEFN; (o) DEFN+ \mathcal{L}_{DWC} .

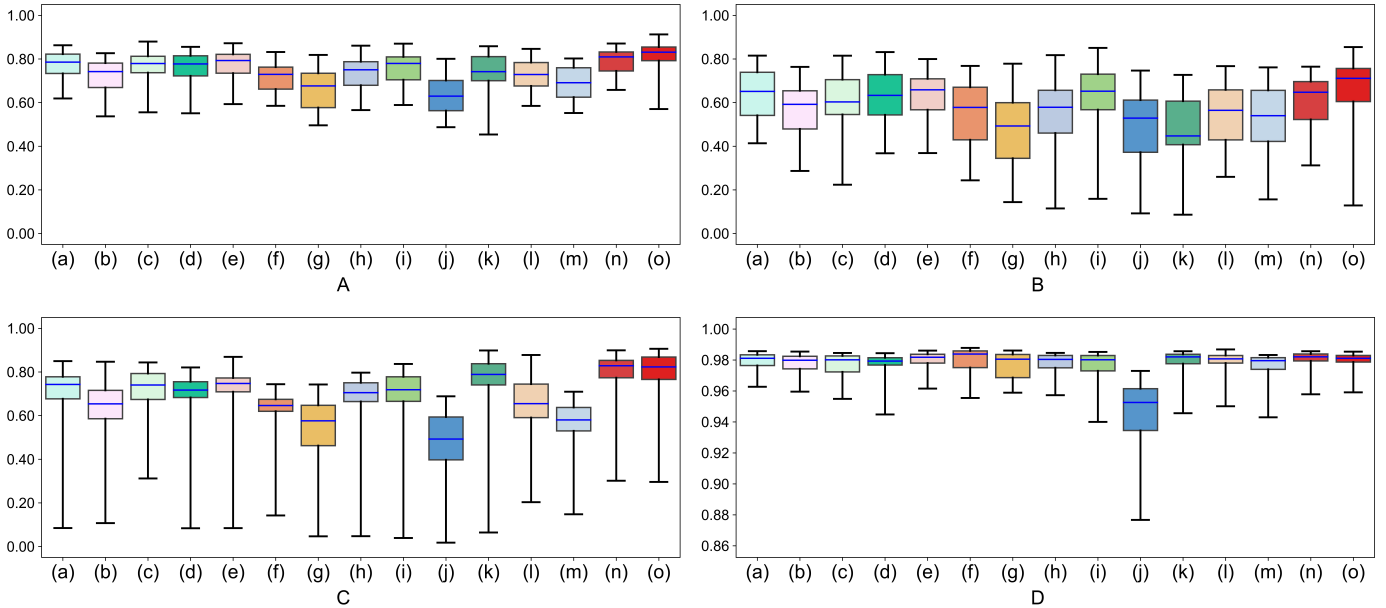


Fig. 8: Box plot showcasing the Dice index from training results using the comprehensive macular hole injection method. The categories are represented as: table A (Average across all classes), table B (Macular Hole), table C (Macular Edema) and table D (Retina). On the x-axis, the models are labeled as: (a) 3D UX-Net; (b) nnFormer; (c) 3D U-Net; (d) SegResNet; (e) Swin UNETR; (f) TransBTS; (g) UNETR; (h) DeepResUNet; (i) ResUNet; (j) HighRes3DNet; (k) MultiResUNet; (l) SegCaps; (m) V-Net; (n) DEFN; (o) DEFN+ \mathcal{L}_{DWC} .

4.3. Experimental setting

All experiments were conducted under the same hardware and software environment. The hardware setup consisted of a desktop computer equipped with eight 4090 graphics cards, an E5-2690V4 CPU, and 256GB of RAM. The project was built on Python 3.9 and PyTorch 2.0.0.

For training, the AdamW (Loshchilov and Hutter, 2017) op-

timizer was used with a learning rate set to 0.0001. The model weights were initialized randomly, and all models underwent the same number of epochs during both the pre-training and fine-tuning phases. The input size for both the ROME-3914 and CARS-30k datasets was $96 \times 96 \times 96$, with a batch size of 1. Leveraging the SRDI strategy, the training data was augmented through flipping, rotating, translating, scaling, adding Gaussian

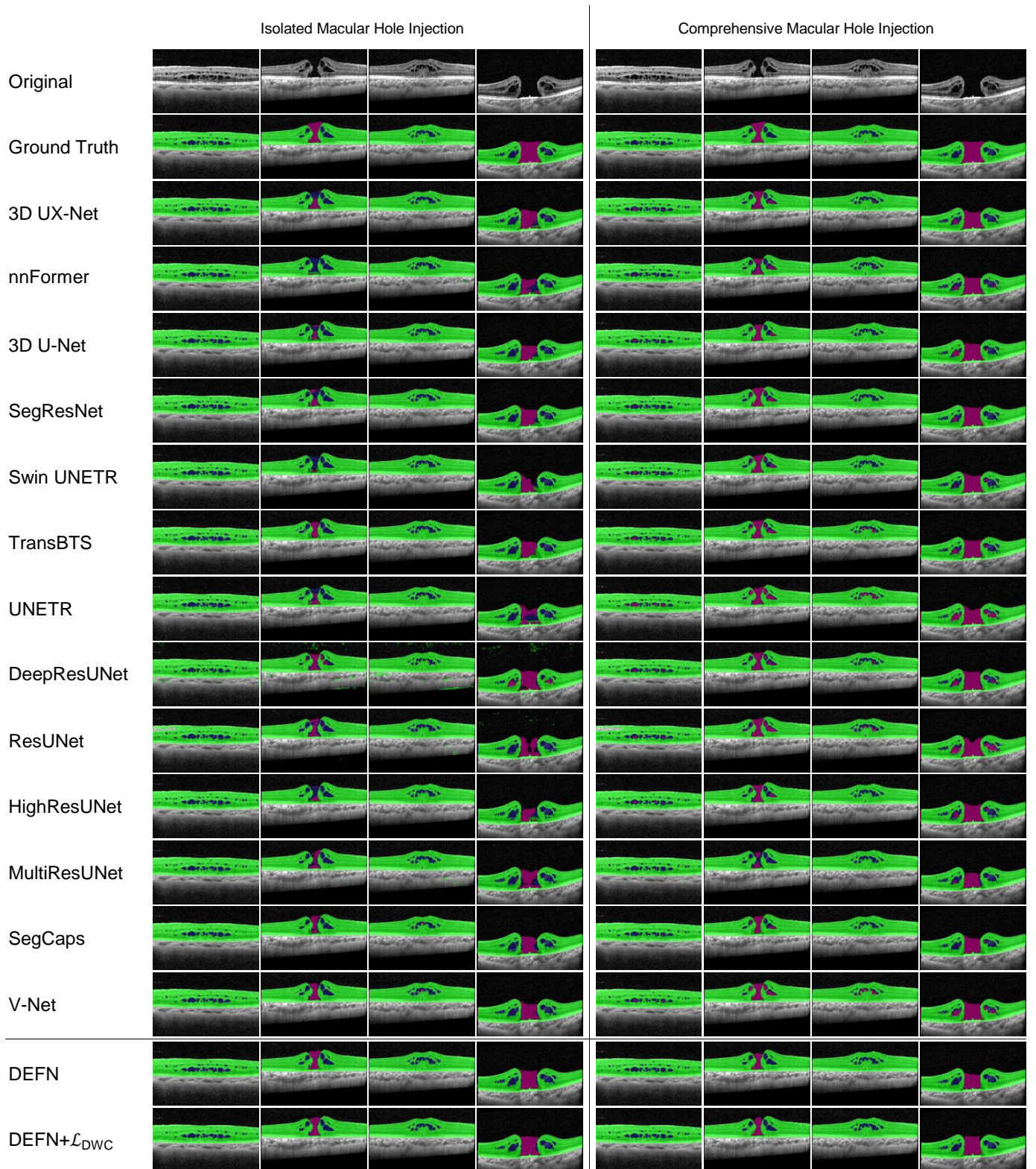


Fig. 9: A few segmentation results of using SRDI, comparison between the proposed DEFN, FEFN+ \mathcal{L}_{DWC} , and previous segmentation models on the ROME-3914 dataset. the left four images showcase the results of the Isolated Macular Hole Injection method, while the right four depict the outcomes of the Comprehensive Macular Hole Injection method. The segmentation result of the retina is shown in green, the segmentation result of the macular edema is shown in blue and the segmentation result of the macular hole is shown in red.

noise, and random histogram transformations.

Table 4: Segmentation results of fine-tuning after isolated macular hole injection training, comparing the proposed DEFN, DEFN+ \mathcal{L}_{DWC} , and prior segmentation models. The evaluation spans four classes: All (Average across all classes), MH (Macular Hole), ME (Macular Edema), and RA (Retina). The best values for each metric are highlighted in red, while the second-best values are highlighted in blue, and the values of our model are bolded.

	All					
	mIOU	Dice	ASSD	HD	HD95	AdjRand
3D UX-Net	85.44±0.69	91.34±0.48	2.24±20.13	103.31±759.53	12.03±622.74	91.01±0.49
nnFormer	80.55±0.98	87.72±0.84	1.74±13.33	102.52±2295.59	10.01±477.82	87.30±0.86
3D U-Net	81.26±0.72	88.54±0.44	3.70±16.78	155.41±3111.91	26.46±1114.34	88.15±0.46
SegResNet	83.31±0.88	89.52±0.84	2.69±55.04	162.22±2159.62	7.52±445.69	89.16±0.84
Swin UNETR	85.70±0.81	91.36±0.62	1.45±27.00	128.41±3953.76	6.60±416.38	91.04±0.62
TransBTS	82.33±0.72	89.07±0.72	1.31±14.22	31.44±502.42	6.34±303.74	88.65±0.71
UNETR	81.25±0.90	88.34±0.70	3.34±32.76	179.47±2263.84	15.75±784.57	87.89±0.71
DeepResUNet	70.95±1.21	80.36±1.04	14.82±107.32	230.94±812.94	83.63±2261.08	79.56±1.07
ResUNet	79.45±0.79	86.84±0.65	8.69±81.24	167.30±2682.32	46.54±1252.12	86.46±0.65
HighRes3DNet	53.35±0.92	65.51±1.19	21.55±172.25	260.05±2330.15	130.13±3900.37	63.60±1.21
MultiResUNet	84.42±0.75	90.62±0.57	2.00±29.22	177.00±1616.34	8.37±444.25	90.25±0.58
SegCaps	74.94±0.75	83.85±0.70	1.86±8.28	69.66±1807.42	7.37±272.87	83.28±0.70
V-Net	83.33±0.72	89.88±0.55	2.52±31.34	166.08±2957.80	10.12±627.03	89.49±0.56
DEFN	86.44±0.75	91.91±0.54	1.35±24.46	93.55±3211.91	6.37±422.64	91.60±0.55
DEFN+\mathcal{L}_{DWC}	87.41±0.59	92.66±0.39	1.03±17.83	28.59±555.79	4.98±398.18	92.37±0.40
	MH					
	mIOU	Dice	ASSD	HD	HD95	AdjRand
3D UX-Net	75.26±3.54	84.66±3.02	6.01±174.23	214.39±3722.89	31.95±5586.14	84.52±3.03
nnFormer	71.14±2.99	82.03±2.27	3.49±98.19	163.70±10009.96	24.06±4169.48	81.87±2.29
3D U-Net	69.02±2.72	80.55±1.89	9.87±142.54	215.46±4201.06	74.91±10202.90	80.38±1.91
SegResNet	75.35±3.90	84.57±3.89	4.44±267.86	189.58±7428.30	16.55±3833.81	84.43±3.91
Swin UNETR	77.59±3.61	86.19±3.40	3.47±231.74	178.87±8553.65	15.64±3685.24	86.07±3.41
TransBTS	74.38±2.85	84.36±2.36	2.55±117.29	30.05±3696.24	15.17±2719.94	84.22±2.36
UNETR	72.02±3.70	82.36±3.41	7.72±248.03	200.83±5104.73	41.32±6974.08	82.20±3.43
DeepResUNet	49.51±3.80	64.07±4.05	36.56±754.73	282.62±1543.71	204.23±11254.91	63.81±4.05
ResUNet	61.24±4.81	73.63±4.59	25.00±712.63	220.89±3812.95	135.43±11063.90	73.41±4.60
HighRes3DNet	37.27±3.27	51.81±4.43	36.65±979.70	287.16±3768.45	174.29±10931.46	51.52±4.43
MultiResUNet	75.86±3.44	85.12±3.32	4.43±249.22	204.69±4200.27	16.84±3793.80	84.98±3.34
SegCaps	61.72±2.82	75.08±2.17	3.61±62.43	101.73±8763.97	16.90±2488.49	74.91±2.17
V-Net	74.35±3.82	83.92±3.53	6.31±263.65	181.95±8843.46	26.22±5674.55	83.78±3.55
DEFN	78.52±3.58	86.81±3.21	3.29±218.45	149.51±9475.51	15.76±3754.28	86.68±3.23
DEFN+\mathcal{L}_{DWC}	79.91±3.05	87.92±2.45	2.48±159.84	26.01±4073.02	10.93±3554.29	87.81±2.46
	ME					
	mIOU	Dice	ASSD	HD	HD95	AdjRand
3D UX-Net	83.04±1.34	90.34±0.61	0.58±2.66	69.76±3865.88	3.11±118.48	90.20±0.61
nnFormer	73.05±5.10	82.41±5.46	1.52±36.31	124.04±3066.41	4.87±320.49	82.18±5.46
3D U-Net	77.11±2.56	86.25±1.78	1.01±4.94	124.63±3869.52	3.42±135.27	86.06±1.77
SegResNet	76.87±4.83	85.17±5.35	3.44±387.53	97.61±4197.47	4.94±475.78	84.99±5.33
Swin UNETR	81.56±3.01	88.94±2.04	0.73±4.56	75.49±3635.10	3.12±119.57	88.80±2.04
TransBTS	75.35±4.59	84.25±5.23	1.18±30.10	51.23±2419.43	2.78±59.80	84.05±5.21
UNETR	74.62±3.74	84.13±3.19	1.98±13.17	131.76±2899.13	4.81±274.49	83.92±3.19
DeepResUNet	68.82±4.09	79.87±3.95	3.61±45.69	171.75±3991.40	20.92±2876.50	79.59±3.94
ResUNet	79.31±1.45	88.01±0.75	0.86±2.36	120.45±4001.02	3.16±122.12	87.84±0.75
HighRes3DNet	37.33±2.47	52.58±3.77	15.76±103.16	241.58±7270.03	114.41±3309.34	51.95±3.68
MultiResUNet	79.69±2.55	87.90±1.49	1.32±7.80	124.91±3548.70	7.21±556.33	87.71±1.50
SegCaps	66.92±4.24	78.43±4.89	1.55±31.69	85.23±3744.13	3.81±50.65	78.16±4.88
V-Net	78.08±2.32	86.95±1.40	0.99±3.17	121.14±3543.81	3.08±117.86	86.74±1.42
DEFN	82.69±2.22	89.88±1.22	0.63±2.99	87.53±3997.39	2.30±35.01	89.73±1.22
DEFN+\mathcal{L}_{DWC}	84.14±1.56	90.98±0.80	0.47±2.27	48.72±2369.76	2.96±114.79	90.84±0.80
	RA					
	mIOU	Dice	ASSD	HD	HD95	AdjRand
3D UX-Net	98.02±0.01	99.00±0.00	0.14±0.01	25.79±2205.69	1.04±0.06	98.32±0.01
nnFormer	97.47±0.02	98.71±0.01	0.22±0.07	19.82±1584.62	1.10±0.11	97.85±0.02
3D U-Net	97.65±0.01	98.81±0.00	0.21±0.03	126.13±8564.66	1.06±0.10	98.00±0.01
SegResNet	97.70±0.01	98.84±0.00	0.19±0.02	199.48±2388.08	1.08±0.10	98.05±0.01
Swin UNETR	97.95±0.01	98.96±0.00	0.15±0.01	130.85±11089.92	1.04±0.06	98.26±0.01
TransBTS	97.26±0.02	98.61±0.00	0.19±0.01	13.04±100.43	1.05±0.07	97.68±0.02
UNETR	97.12±0.02	98.54±0.01	0.31±0.23	205.82±5221.38	1.11±0.26	97.55±0.02
DeepResUNet	94.53±0.22	97.15±0.07	4.29±16.92	238.45±602.48	25.76±2050.40	95.26±0.20
ResUNet	97.80±0.01	98.89±0.00	0.21±0.02	160.56±9208.11	1.04±0.06	98.14±0.01
HighRes3DNet	85.47±0.13	92.13±0.05	12.25±32.82	251.40±331.35	101.70±4286.03	87.34±0.13
MultiResUNet	97.72±0.01	98.84±0.00	0.27±0.03	201.41±1800.18	1.05±0.10	98.07±0.01
SegCaps	96.17±0.01	98.04±0.00	0.41±0.61	22.01±1722.15	1.40±0.71	96.76±0.01
V-Net	97.58±0.02	98.77±0.01	0.25±0.04	195.16±6335.32	1.05±0.07	97.94±0.02
DEFN	98.10±0.01	99.04±0.00	0.13±0.01	43.61±5768.94	1.04±0.06	98.39±0.01
DEFN+\mathcal{L}_{DWC}	98.20±0.01	99.09±0.00	0.13±0.01	11.03±46.81	1.04±0.06	98.47±0.01

Table 5: Segmentation results of fine-tuning after comprehensive macular hole injection training, comparing the proposed DEFN, DEFN+ \mathcal{L}_{DWC} , and prior segmentation models. The evaluation spans four classes: All (Average across all classes), MH (Macular Hole), ME (Macular Edema), and RA (Retina). The best values for each metric are highlighted in red, while the second-best values are highlighted in blue, and the values of our model are bolded.

	All					
	mIOU	Dice	ASSD	HD	HD95	AdjRand
3D UX-Net	83.91±0.35	90.61±0.23	1.56±4.89	110.23±1814.31	5.89±214.34	90.25±0.23
nnFormer	70.75±1.70	79.61±1.73	4.00±60.69	49.58±1747.17	16.21±723.87	79.01±1.78
3D U-Net	82.76±0.70	89.56±0.45	1.62±17.61	103.89±1926.92	6.84±394.17	89.17±0.47
SegResNet	82.96±0.86	89.36±0.73	2.58±34.61	108.66±3407.80	10.26±574.79	88.96±0.74
Swin UNETR	84.21±0.90	90.12±0.87	2.67±27.55	117.71±1417.52	14.85±723.80	89.77±0.87
TransBTS	79.53±0.83	87.05±0.78	3.28±39.13	100.79±2320.48	12.39±593.21	86.59±0.79
UNETR	80.38±0.89	87.74±0.72	3.94±35.15	183.50±2414.01	22.30±924.89	87.30±0.73
DeepResUNet	75.77±1.05	84.15±0.89	8.77±73.14	148.71±1863.88	53.50±1854.19	83.70±0.89
ResUNet	81.61±0.90	88.39±0.78	5.25±45.02	134.87±2187.53	29.02±1107.79	88.01±0.78
HighRes3DNet	73.96±1.12	82.84±0.96	9.81±96.44	191.90±1523.89	51.92±2725.59	82.28±0.97
MultiResUNet	82.60±0.70	89.45±0.52	2.12±5.91	200.55±971.91	6.89±192.52	89.07±0.53
SegCaps	81.08±0.83	88.04±0.77	1.88±21.45	73.85±2277.20	7.19±426.01	87.64±0.77
V-Net	78.73±0.86	86.49±0.77	6.80±62.50	180.47±3031.37	39.77±1674.51	86.03±0.78
DEFN	86.56±0.69	92.05±0.51	1.15±27.21	29.85±568.33	5.06±379.60	91.75±0.51
DEFN+\mathcal{L}_{DWC}	86.95±0.37	92.61±0.16	0.40±0.61	28.38±403.42	2.54±47.22	92.30±0.16
	MH					
	mIOU	Dice	ASSD	HD	HD95	AdjRand
3D UX-Net	75.09±0.53	85.58±0.24	2.95±6.87	187.03±7027.28	9.13±1001.82	85.46±0.24
nnFormer	52.81±5.77	65.66±6.73	9.37±517.05	58.11±6344.11	40.26±6371.02	65.48±6.71
3D U-Net	72.74±2.95	83.14±2.28	3.66±142.64	191.14±5960.32	13.33±3182.41	82.98±2.31
SegResNet	74.92±3.90	84.26±3.69	5.78±289.42	139.53±10092.64	25.30±5143.77	84.12±3.70
Swin UNETR	74.97±3.57	84.46±3.48	6.64±228.08	213.48±3273.29	41.05±6557.17	84.31±3.50
TransBTS	69.86±3.31	81.05±3.30	6.03±246.79	161.00±8552.46	27.59±4798.36	80.88±3.32
UNETR	69.82±3.60	80.88±3.47	9.63±271.80	211.87±4163.06	57.85±8189.02	80.71±3.48
DeepResUNet	57.83±3.79	71.50±3.68	22.31±523.57	211.11±4598.03	134.40±10384.70	71.24±3.69
ResUNet	70.11±3.96	80.89±3.98	13.48±370.79	215.23±4357.20	76.63±10172.68	80.73±3.99
HighRes3DNet	60.62±4.09	73.56±3.99	21.77±556.71	202.87±5130.97	111.02±11404.21	73.33±4.00
MultiResUNet	73.84±1.96	84.32±1.33	4.45±47.59	225.81±1510.84	13.19±1500.44	84.17±1.33
SegCaps	74.36±3.12	84.24±2.66	4.07±184.99	132.31±10342.19	16.97±3827.71	84.10±2.67
Vnet	67.20±3.79	78.87±3.66	14.84±370.83	192.34±8709.90	97.53±10596.38	78.70±3.67
DEFN	78.41±3.50	86.77±3.21	2.84±243.95	27.43±3948.28	11.11±3372.63	86.66±3.22
DEFN+\mathcal{L}_{DWC}	79.47±0.90	88.31±0.42	0.79±5.02	21.10±1216.19	4.90±407.06	88.19±0.42
	ME					
	mIOU	Dice	ASSD	HD	HD95	AdjRand
3D UX-Net	78.91±2.73	87.38±1.95	1.57±44.18	122.75±3368.57	7.49±1542.64	87.21±1.95
nnFormer	63.10±4.90	75.02±5.52	2.28±75.49	59.95±2819.61	6.65±374.84	74.68±5.53
3D U-Net	77.89±2.58	86.73±1.57	1.04±12.54	99.49±4453.71	6.16±908.30	86.52±1.60
SegResNet	76.44±4.41	85.07±4.41	1.77±23.06	123.45±3520.33	4.42±183.32	84.88±4.40
Swin UNETR	79.78±5.05	86.98±5.51	1.23±27.26	120.47±3989.56	2.47±45.58	86.81±5.50
TransBTS	71.56±4.70	81.57±5.21	3.61±167.50	124.40±4195.57	8.36±1547.85	81.32±5.21
UNETR	73.97±3.76	83.68±3.31	1.97±31.87	131.50±2609.77	7.95±1430.94	83.46±3.31
DeepResUNet	72.00±3.97	82.23±3.92	3.78±81.39	147.19±2844.19	25.05±2612.54	82.00±3.91
ResUNet	77.07±4.39	85.47±3.99	2.06±41.54	133.34±2782.57	9.39±1497.18	85.29±3.98
HighRes3DNet	64.56±4.19	76.64±4.59	6.73±172.86	144.07±2910.58	43.53±3808.31	76.32±4.58
MultiResUNet	76.25±3.90	85.19±3.39	1.57±13.56	145.06±2217.77	6.44±505.19	84.97±3.39
SegCaps	71.36±5.23	81.14±5.57	1.38±28.54	76.56±3794.46	3.46±59.81	80.92±5.56
V-Net	71.76±4.11	82.00±4.31	5.06±265.23	137.95±2911.54	20.67±2769.70	81.75±4.31
DEFN	83.18±1.70	90.34±0.85	0.47±2.66	46.85±2522.22	3.03±121.69	90.20±0.84
DEFN+\mathcal{L}_{DWC}	83.28±1.33	90.47±0.57	0.29±0.09	48.76±2777.97	1.67±2.61	90.33±0.58
	RA					
	mIOU	Dice	ASSD	HD	HD95	AdjRand
3D UX-Net	97.73±0.01	98.85±0.00	0.17±0.01	20.91±2298.75	1.04±0.06	98.07±0.01
nnFormer	96.34±0.04	98.13±0.01	0.35±0.14	30.69±2480.51	1.71±5.69	96.88±0.04
3D U-Net	97.66±0.02	98.81±0.00	0.16±0.01	21.04±871.42	1.04±0.06	98.00±0.02
SegResNet	97.52±0.02	98.74±0.00	0.19±0.01	63.00±6453.83	1.06±0.10	97.89±0.01
Swin UNETR	97.87±0.01	98.92±0.00	0.15±0.01	19.17±681.19	1.04±0.06	98.19±0.01
TransBTS	97.15±0.03	98.55±0.01	0.21±0.03	16.95±188.10	1.21±0.66	97.56±0.03
UNETR	97.34±0.02	98.65±0.01	0.22±0.02	207.12±3859.17	1.11±0.26	97.73±0.02
DeepResUNet	97.49±0.01	98.73±0.00	0.21±0.02	87.83±6477.26	1.05±0.10	97.87±0.01
ResUNet	97.65±0.01	98.81±0.00	0.20±0.03	56.05±6349.18	1.04±0.06	98.00±0.01
HighRes3DNet	96.69±0.03	98.31±0.01	0.93±0.61	228.76±1165.60	1.22±0.28	97.19±0.02
MultiResUNet	97.71±0.01	98.84±0.00	0.34±0.27	230.78±1051.25	1.05±0.10	98.05±0.01
SegCaps	97.52±0.01	98.74±0.00	0.19±0.03	12.69±66.24	1.15±0.28	97.90±0.01
V-Net	97.24±0.03	98.59±0.01	0.51±0.11	211.11±3817.70	1.12±0.13	97.64±0.03
DEFN	98.10±0.01	99.04±0.00	0.14±0.01	15.27±605.97	1.04±0.06	98.39±0.01
DEFN+\mathcal{L}_{DWC}	98.09±0.01	99.03±0.00	0.14±0.01	15.28±600.80	1.04±0.06	98.38±0.01

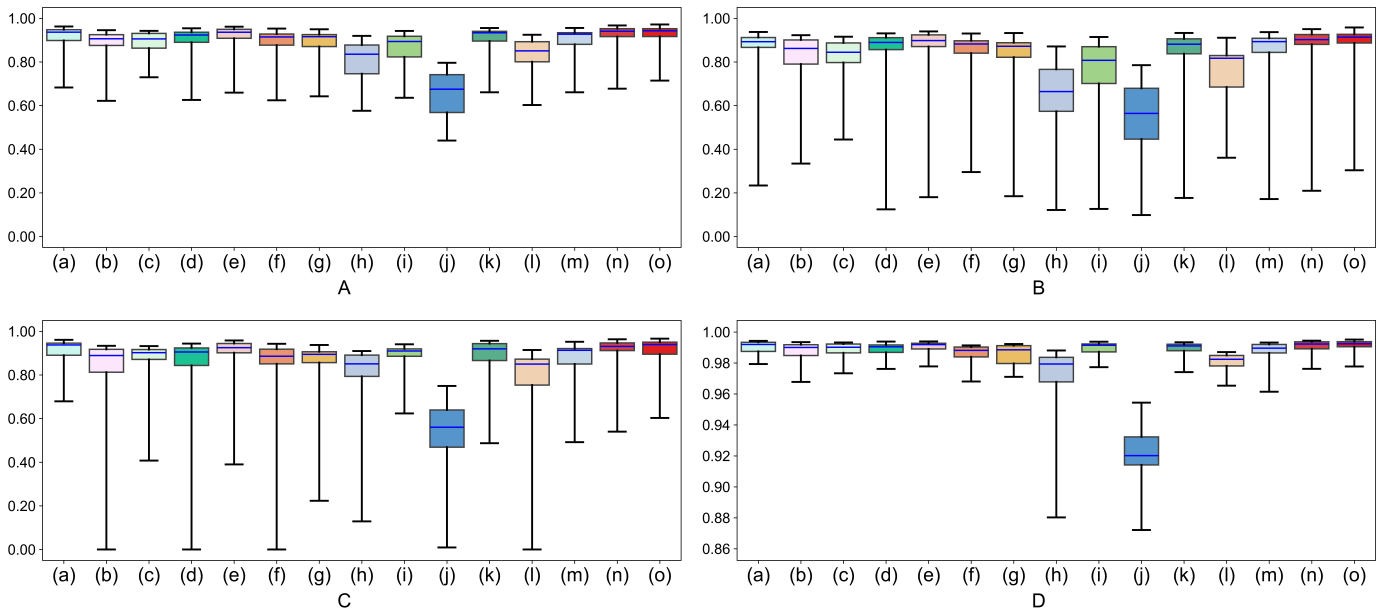


Fig. 10: Box plot showcasing the Dice index from fine-tuning results after isolated macular hole injection training. The categories are denoted as: table A (Average across all classes), table B (Macular Hole), table C (Macular Edema) and table D (Retina). Along the x-axis, the models are marked as: (a) 3D UX-Net; (b) nnFormer; (c) 3D U-Net; (d) SegResNet; (e) Swin UNETR; (f) TransBTS; (g) UNETR; (h) DeepResUNet; (i) ResUNet; (j) HighRes3DNet; (k) MultiResUNet; (l) SegCaps; (m) V-Net; (n) DEFN; (o) DEFN+ \mathcal{L}_{DWC} .

4.4. SRDI augmentation for enhanced dataset transferability in retinal studies

In this section, we showcase the performance of our model on the ROME-3914 test dataset, having trained it on the CARS-30k dataset with two distinct SRDI data augmentation techniques. We also compare our results to those achieved by other methods. Furthermore, in order to understand the influence of various loss functions on the model’s adaptability, we utilized both \mathcal{L}_{DiceCE} and \mathcal{L}_{DWC} as optimization strategies.

4.4.1. Training results using isolated macular hole injection

The results of using the isolated Macular hole injection strategy to process the CARS-30k dataset and perform training, then testing on the ROME-3914 dataset, demonstrated DEFN’s good segmentation performance, as shown in Table.2 and Fig.7. Compared to all other models, DEFN showed excellent overall transfer performance. When using \mathcal{L}_{DiceCE} as the loss function together with other networks, DEFN showed excellent segmentation ability in the average of all categories and achieved competitive performance in mIOU, Dice, and AdjRand indicators. The mIOU and Dice for the macular hole segmentation were more than 10% higher than other networks, demonstrating DEFN’s strong ability in segmenting categories with less obvious features, thanks to the deep information extraction ability of FuGH and the outstanding feature extraction and noise removal ability of S3DSA. After applying \mathcal{L}_{DWC} in DEFN, DEFN’s various indicators were significantly improved, among which the segmentation ability improvement for the macular edema was most obvious, with mIOU and Dice increased by 2.9% and 2.59% respectively. This was mainly due to the joint effect of \mathcal{L}_{Focal} and $\mathcal{L}_{Boundary}$ fused in \mathcal{L}_{DWC} , which optimized the segmentation performance for small targets and boundaries that are

easy to confuse. The mIOU, Dice, ASSD, HD, HD95, and AdjRand indicators for the macular hole category, macular edema category, and the average of all categories all ranked first among all networks. The overall mIOU and Dice even reached 67.39% and 76.71%, reflecting the help of \mathcal{L}_{DWC} for region segmentation. Meanwhile, the outstanding advantages of the three indicators ASSD, HD, and HD95 also showed that our network performed well in segmentation details. The specific segmentation effect is shown in Fig.9.

4.4.2. Training results using comprehensive macular hole injection

The results of using the comprehensive macular hole injection strategy for data processing and training on the CARS-30k dataset, and testing on the real ROME-3914 macular hole dataset, are shown in Table.3 and Fig.8. In comparison with other models, DEFN showed excellent transfer ability. Without using the \mathcal{L}_{DWC} optimization strategy, DEFN’s mIOU and Dice averages of all categories were significantly higher than other models, especially in the macular edema category, where the mIOU and Dice indicators were 3.92% and 3.54% higher than the best-performing models, respectively. Distinguishing the macular edema and the macular hole is a challenge of the task, as shown in Fig 9, the DEFN model can more accurately distinguish the macular hole and the macular edema. Specifically, the joint use of the FuGH module and HSE module strengthened DEFN’s understanding of the regularity of the data and effectively suppressed interfering noise and unnecessary feature channels, thus showing superior transfer performance. While using the \mathcal{L}_{DWC} transformation, DEFN’s various indicators were significantly improved, with the Dice average of all categories reaching 80.92%, and the model’s ASSD, HD, and

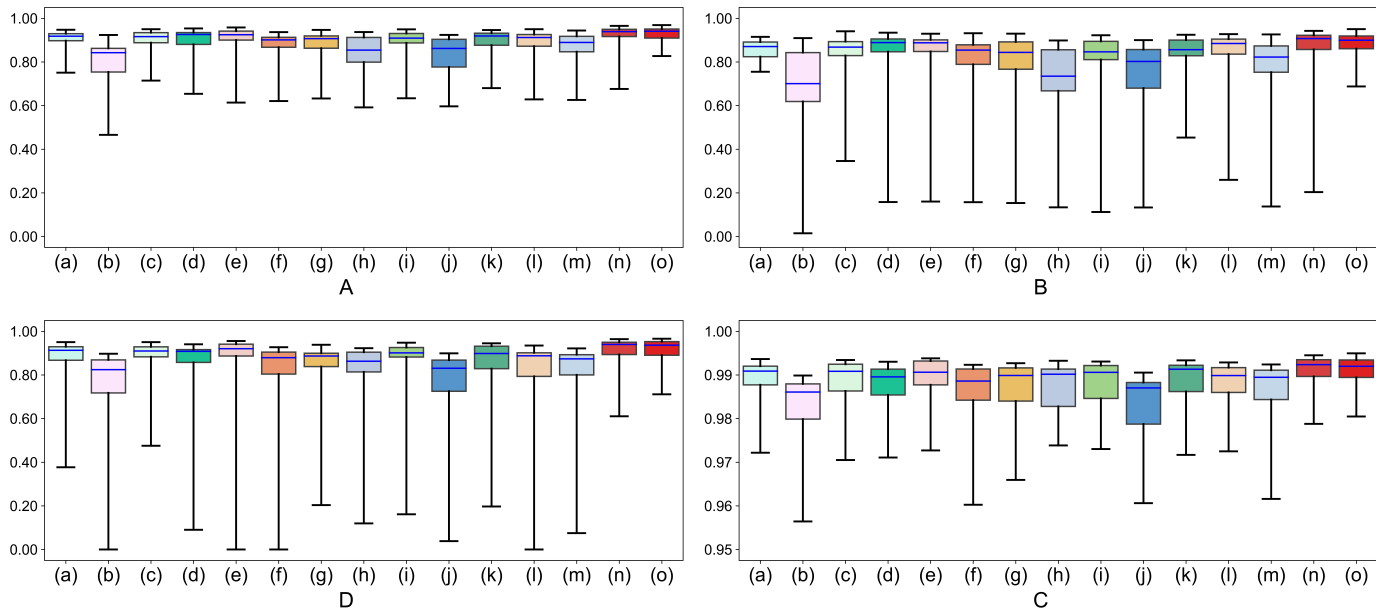


Fig. 11: Box plot showcasing the Dice index from fine-tuning results after comprehensive macular hole injection training. The categories are denoted as: table A (Average across all classes), table B (Macular Hole), table C (Macular Edema) and table D (Retina). Along the x-axis, the models are marked as: (a) 3D UX-Net; (b) nnFormer; (c) 3D U-Net; (d) SegResNet; (e) Swin UNETR; (f) TransBTS; (g) UNETR; (h) DeepResUNet; (i) ResUNet; (j) HighRes3DNet; (k) MultiResUNet; (l) SegCaps; (m) V-Net; (n) DEFN; (o) DEFN+ \mathcal{L}_{DWC} .

HD95 metrics also improved significantly. This shows that in the early training stage, we paid more attention to regional accuracy, and as the training progressed, increasing the focus on boundary accuracy of segmentation with the \mathcal{L}_{DWC} transformation could significantly improve the model’s segmentation performance, as shown in the segmentation effect of Fig.9.

4.5. fine-tuning with ROME-3914 for enhance SRDI model performance

Using the pre-trained models that were developed with two unique SRDI data augmentation approaches, we continued our training on the REMO-3914 dataset and obtained the segmentation results for the ROME-3914 test dataset, which we then compared with other methods. Same as in Section 4.4, our training leveraged both \mathcal{L}_{DiceCE} and \mathcal{L}_{DWC} optimization strategies, allowing us to assess the influence of the loss tied to the DWC transformation strategy on the model’s performance.

4.5.1. fine-tuning results after isolated macular hole injection training

Implementing the injection macular hole isolated strategy for data augmentation and pre-training on the CARS-30k dataset, and further fine-tuning on the ROME-3914 dataset, the resulting segmentation ability metrics are shown in Table.4 and Fig.10. DEFN displays more comprehensive and good performance in fine-tuning, surpassing other models. Without the use of \mathcal{L}_{DWC} , DEFN surpasses other models on the mIOU, Dice, ASSD, and AdjRand indices for the macular hole, the retinal, and all categories on average. In the important and challenging category of the macular hole, its mIOU and Dice scores achieve 78.52% and 86.81% respectively, with mIOU 0.93% higher than the best other models, while AdjRand exceeds other

models by at least 0.61%. This implies that the FuGH, S3DSA, and HSE modules in the DEFN have superior overall segmentation results in transfer and fine-tuning. Upon the inclusion of the \mathcal{L}_{DWC} optimization strategy, all indices further improve. For instance, the mIOU and Dice scores for the macular hole category increase by 1.39% and 1.11% respectively, while the ASSD, HD, and HD95 metrics also improve, validating the advantages of utilizing \mathcal{L}_{DWC} as an optimization strategy for the model’s overall segmentation and detail processing. In conclusion, DEFN attains commendable scores on essentially all indices for the macular hole, the macular edema, and the retina categories, demonstrating significant competitiveness. The illustration of the segmentation effect is shown in Fig.12.

4.5.2. fine-tuning results after comprehensive macular hole injection training

On the basis of data processing and pre-training using the comprehensive macular hole injection strategy on the CARS-30k dataset, the results after fine-tuning on the ROME-3914 dataset are shown in Table5 and Fig.11. Compared to other models, DEFN exhibits excellent performance overall. Without the optimization of \mathcal{L}_{DWC} , DEFN surpasses other models on most indicators. As can be seen from Table.5 and Fig.11, DEFN can accurately distinguish the macular hole and the macular edema with distinctive features, and it also performs well on images with much interference, such as a large amount of noise and image defects, thanks to the excellent denoising ability of the FuGH module and the spatial attention mechanism of the S3DSA module. Moreover, the use of the HSE module for feature channel selection allows DEFN to predict the upper boundary in a category like the macular hole, the Dice score reaching 86.77%, outperforming the best other models

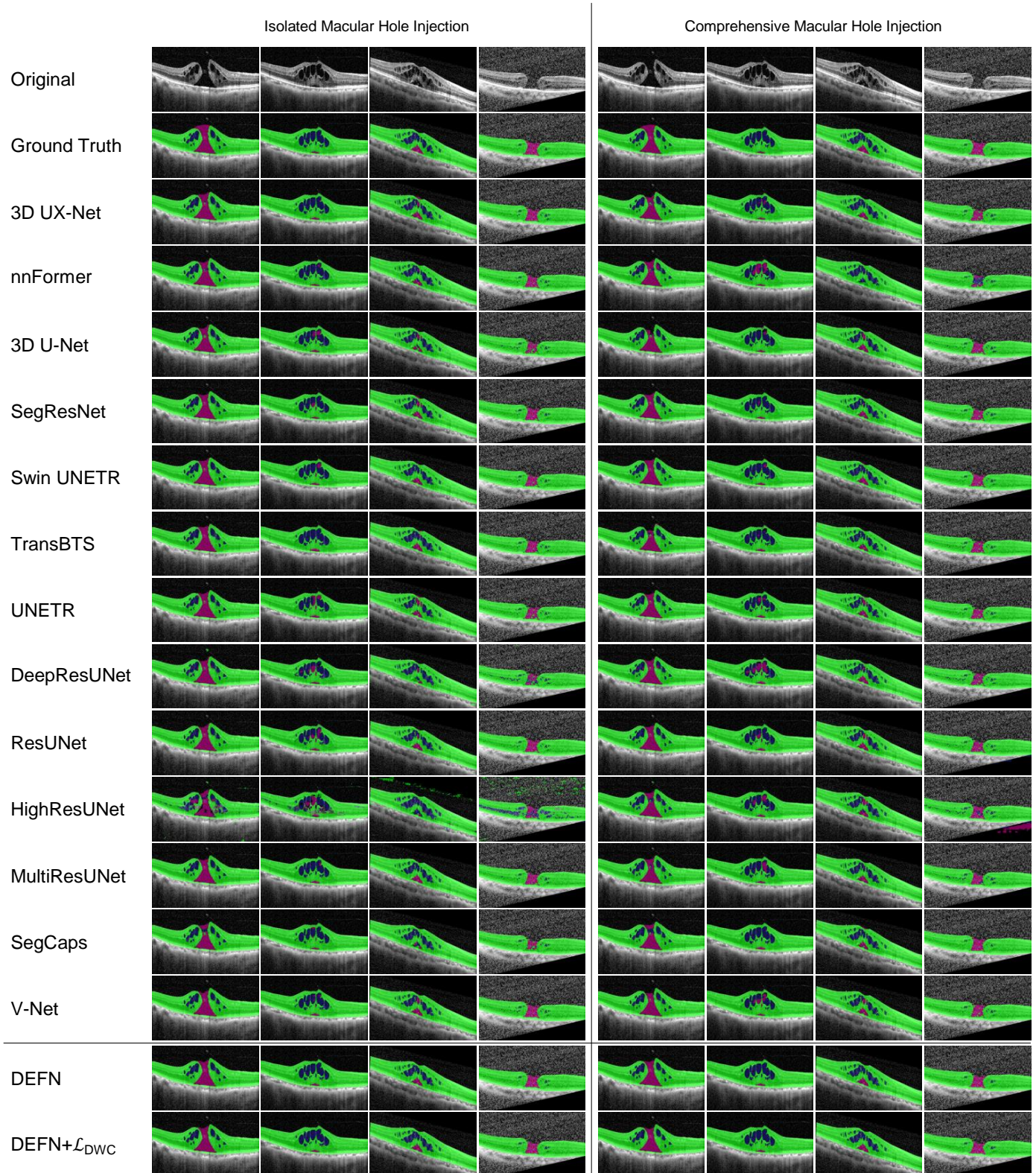


Fig. 12: A few segmentation results of fine-tuning after SRDI training, comparison between the proposed DEFN, FEFN+ \mathcal{L}_{DWC} and previous segmentation models on the ROME-3914 dataset. the left four images showcase the results of the Isolated Macular Hole Injection method, while the right four depict the outcomes of the Comprehensive Macular Hole Injection method. The segmentation result of the retina is shown in green, the segmentation result of the macular edema is shown in blue and the segmentation result of the macular hole is shown in red.

by 1.19%. Besides, FuGH is successful in discovering patterns within the data and significantly reducing noise, thus allowing

DEFN to demonstrate excellent performance in terms of segmentation boundary precision. It outperforms other models in

Table 6: Ablation study on the backbone and modules of DEFN and our methods, including DEFN (DEFN backbone), HSE (Harmonic Squeeze-and-Excitation Module), FuGH (Fourier Group Harmonics), IMHI (Isolated Macular Hole Injection), CMHI (Comprehensive Macular Hole Injection) and DWC (DynamicWeight-Compose). The best values for each metric are highlighted in red, while the second-best values are highlighted in blue.

						All					
DEFN	HSE	FuGH	IMHI	CMHI	DWC	mIOU	Dice	ASSD	HD	HD95	AdjRand
✓						84.24±0.85	90.20±0.77	1.49±27.67	88.16±3011.24	6.60±424.73	89.84±0.78
✓	✓					85.62±0.86	91.20±0.69	1.42±27.72	88.96±2889.36	6.39±419.59	90.87±0.69
✓	✓	✓				85.83±0.75	91.43±0.60	1.70±30.90	83.17±1971.82	8.88±553.67	91.11±0.60
✓	✓	✓	✓			86.44±0.75	91.91±0.54	1.35±24.46	93.55±3211.91	6.37±422.64	91.60±0.55
✓	✓	✓		✓		86.56±0.69	92.05±0.51	1.15±27.21	29.85±568.33	5.06±379.60	91.75±0.51
✓	✓	✓			✓	86.60±0.67	92.08±0.54	1.29±30.07	43.32±1776.56	5.04±381.78	91.79±0.54
✓	✓	✓	✓		✓	87.41±0.59	92.66±0.39	1.03±17.83	28.59±555.79	4.98±398.18	92.37±0.40
✓	✓	✓		✓	✓	86.95±0.37	92.61±0.16	0.40±0.61	28.38±403.42	2.54±47.22	92.30±0.16
						MH					
DEFN	HSE	FuGH	IMHI	CMHI	DWC	mIOU	Dice	ASSD	HD	HD95	AdjRand
✓						76.07±3.57	85.20±3.39	3.58±245.70	159.27±7645.39	16.49±3761.83	85.07±3.40
✓	✓					77.39±3.40	86.15±3.13	3.19±243.16	127.54±10683.79	15.97±3754.56	86.02±3.14
✓	✓	✓				77.96±3.71	86.39±3.52	3.80±262.41	113.57±10590.44	18.40±4430.92	86.27±3.53
✓	✓	✓	✓			78.52±3.58	86.81±3.21	3.29±218.45	149.51±9475.51	15.76±3754.28	86.68±3.23
✓	✓	✓		✓		78.41±3.50	86.77±3.21	2.84±243.95	27.43±3948.28	11.11±3372.63	86.66±3.22
✓	✓	✓			✓	78.18±3.73	86.52±3.68	3.19±270.26	50.19±7128.57	11.06±3386.87	86.40±3.69
✓	✓	✓	✓		✓	79.91±3.05	87.92±2.45	2.48±159.84	26.01±4073.02	10.93±3554.29	87.81±2.46
✓	✓	✓		✓	✓	79.47±0.90	88.31±0.42	0.79±5.02	21.10±1216.19	4.90±407.06	88.19±0.42
						ME					
DEFN	HSE	FuGH	IMHI	CMHI	DWC	mIOU	Dice	ASSD	HD	HD95	AdjRand
✓						78.90±4.77	86.53±5.04	0.73±9.33	67.18±3614.81	2.28±31.56	86.36±5.03
✓	✓					81.57±4.22	88.50±3.83	0.88±13.46	103.80±4435.21	2.16±32.35	88.36±3.82
✓	✓	✓				81.61±3.06	88.96±2.18	1.17±28.95	115.34±3766.97	7.21±1484.02	88.81±2.18
✓	✓	✓	✓			82.69±2.22	89.88±1.22	0.63±2.99	87.53±3997.39	2.30±35.01	89.73±1.22
✓	✓	✓		✓		83.18±1.70	90.34±0.85	0.47±2.66	46.85±2522.22	3.03±121.69	90.20±0.84
✓	✓	✓			✓	83.49±1.21	90.67±0.56	0.55±2.31	55.67±2798.92	3.02±120.29	90.53±0.55
✓	✓	✓	✓		✓	84.14±1.56	90.98±0.80	0.47±2.27	48.72±2369.76	2.96±114.79	90.84±0.80
✓	✓	✓		✓	✓	83.28±1.33	90.47±0.57	0.29±0.09	48.76±2777.97	1.67±2.61	90.33±0.58
						RA					
DEFN	HSE	FuGH	IMHI	CMHI	DWC	mIOU	Dice	ASSD	HD	HD95	AdjRand
✓						97.74±0.01	98.85±0.00	0.16±0.01	38.03±5653.30	1.04±0.06	98.07±0.01
✓	✓					97.91±0.01	98.94±0.00	0.17±0.04	35.54±2976.33	1.04±0.06	98.23±0.01
✓	✓	✓				97.92±0.01	98.95±0.00	0.14±0.01	20.59±673.66	1.04±0.06	98.24±0.01
✓	✓	✓	✓			98.10±0.01	99.04±0.00	0.13±0.01	43.61±5768.94	1.04±0.06	98.39±0.01
✓	✓	✓		✓		98.10±0.01	99.04±0.00	0.14±0.01	15.27±605.97	1.04±0.06	98.39±0.01
✓	✓	✓			✓	98.15±0.01	99.06±0.00	0.13±0.01	24.10±3707.53	1.04±0.06	98.43±0.01
✓	✓	✓	✓		✓	98.20±0.01	99.09±0.00	0.13±0.01	11.03±46.81	1.04±0.06	98.47±0.01
✓	✓	✓		✓	✓	98.09±0.01	99.03±0.00	0.14±0.01	15.28±600.80	1.04±0.06	98.38±0.01

the ASSD, HD, HD95, and AdjRand metrics, scoring optimally across most indicators. Moreover, with the application of the \mathcal{L}_{DWC} optimization strategy, all the metrics show a significant improvement, like the Dice score increase 1.54% in the macular hole category, while ASSD, HD, HD95, and other indices have decreased, thus validating the effectiveness of the \mathcal{L}_{DWC} optimization strategy. The segmentation result is illustrated in Fig.12.

4.6. Ablation study

To validate the authenticity and reliability of our method in improving segmentation performance, we conducted ablation studies to evaluate the impact of using the HSE branch, FuGH

module, SRDI method, and \mathcal{L}_{DWC} transformation strategy on model performance. It can be easily concluded from Table.6 and Fig.13 that the branch of DEFN is indispensable. Once the HSE branch is removed, all indicators will see a significant decline, such as the average mIOU and Dice of all categories decreasing by 1.38% and 1% respectively, proving the fundamental role of HSE branches in ensuring segmentation capabilities. At the same time, the FuGH module and the two SRDI expansion strategies of CARS-30k for fine-tuning are helpful for the segmentation performance of the model, and the performance of the two SRDI expansion strategies is finally equivalent, with only 0.04% difference in the Dice indicator for the macular hole category. In addition, the data also proves the excellent perfor-

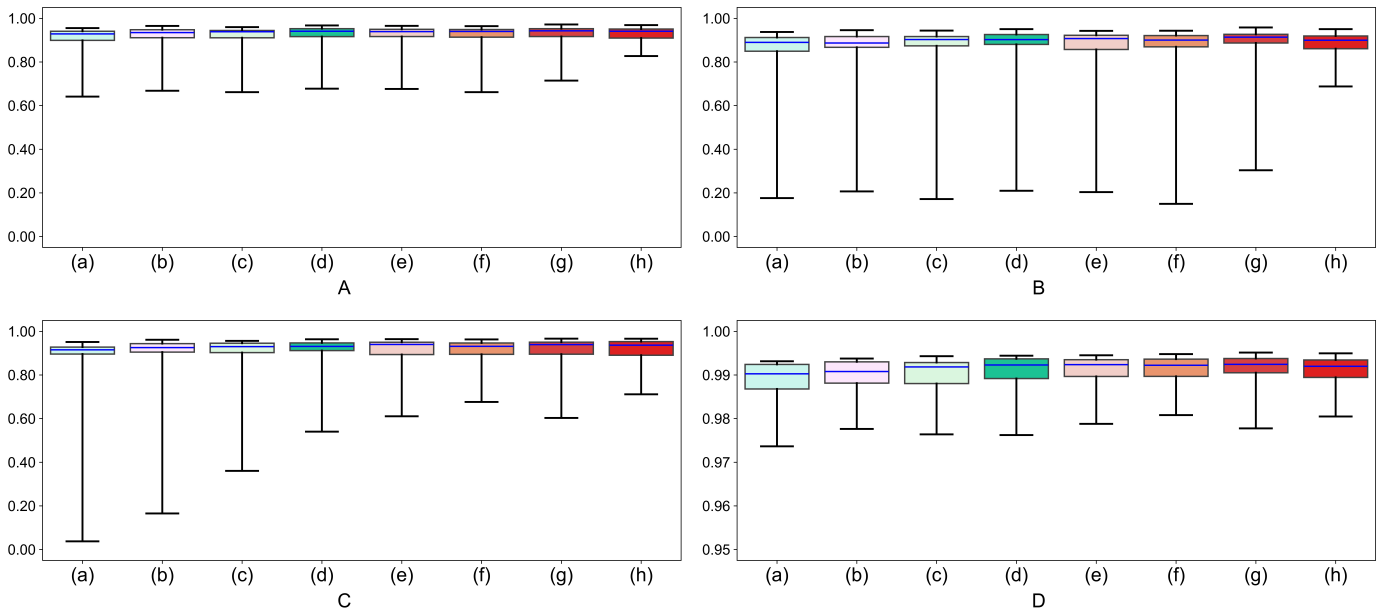


Fig. 13: Box plot showcasing the Dice index from ablation study. The categories are denoted as: table A for the average across all classes, table B for the Macular Hole, table C for the Macular Edema and table D for the Retina. Along the x-axis, the models are marked as: (a) DEFN; (b) DEFN+HSE; (c) DEFN+HSE+FuGH; (d) DEFN+HSE+FuGH+IMHI; (e) DEFN+HSE+FuGH+CMHI; (f) DEFN+HSE+FuGH+DWC; (g) DEFN+HSE+FuGH+IMHI+DWC; (h) DEFN+HSE+FuGH+CMHI+DWC; where DEFN is DEFN backbone, HSE is Harmonic Squeeze-and-Excitation Module, FuGH is Fourier Group Harmonics, IMHI is Isolated Macular Hole Injection, CMHI is Comprehensive Macular Hole Injection and DWC is DynamicWeightCompose.

mance of \mathcal{L}_{DWC} in this task. Without using the SRDI expansion strategy, after applying the \mathcal{L}_{DWC} optimization strategy, the average Dice of all categories was improved by 0.65%, and the average ASSD of all categories decreased from 1.7 to 1.29, further proving the help of the \mathcal{L}_{DWC} optimization strategy in improving regional segmentation and edge detail segmentation of the model.

4.7. 3D reconstruction for retinal

To address the current situation where an intuitive and accurate 3D reconstruction model cannot be obtained due to the lack of a precise and reliable 3D reconstruction method, making it difficult to provide sufficient quantitative indicators to assist doctors in clinical treatment, we proposed a brand new 3D reconstruction scheme for retinal fundus. This 3D reconstruction scheme can provide accurate retinal fundus 3D modeling, allowing patients to more intuitively observe their condition, and provide comprehensive and accurate quantitative indicators according to the ETDRS grid. Doctors can make more accurate and reasonable judgments about the patient's condition based on these quantitative indicators, simplifying the process of condition monitoring. During treatment, these quantitative indicators can also provide reliable guidance for doctors.

4.7.1. 3D reconstruction

This 3D reconstruction method can automatically generate 3D images of the retinal fundus images after segmentation and has designed four rendering schemes to provide different observation perspectives and highlight different focuses based on actual needs. The original 3D reconstruction and results of the four rendering schemes as well as the top view are

shown in Fig.14. Specifically, the steps are: first, generate three-dimensional voxels based on the segmented results, then perform voxel smoothing, and finally generate 3D modeling. Through our testing, it only takes 33s on a single 4090 GPU to complete the 3D reconstruction from the input of a typical sequence, and the usage time is stable for input sequences of any length.

4.7.2. Quantitative index calculation

In order to provide more precise and meaningful quantitative indicators for clinical doctors, we adopted the widely used ETDRS grid in ophthalmology. As shown in Fig.15(a), the grid consists of nine specific regions and three concentric circles:

F (Foveal): represents the central depressed part of the macula, which is the source of human central vision.

IS (Inner Superior): represents the region above the macula center.

II (Inner Inferior): represents the region below the macula center.

IT (Inner Temporal): represents the region toward the nasal side of the macula center.

IN (Inner Nasal): represents the region toward the temporal side of the macula center.

OS (Outer Superior): represents the region outside the upper region of the macula center.

OI (Outer Inferior): represents the region outside the lower region of the macula center.

OT (Outer Temporal): represents the region outside the nasal side region of the macula center.

ON (Outer Nasal): represents the region outside the temporal side region of the macula center.

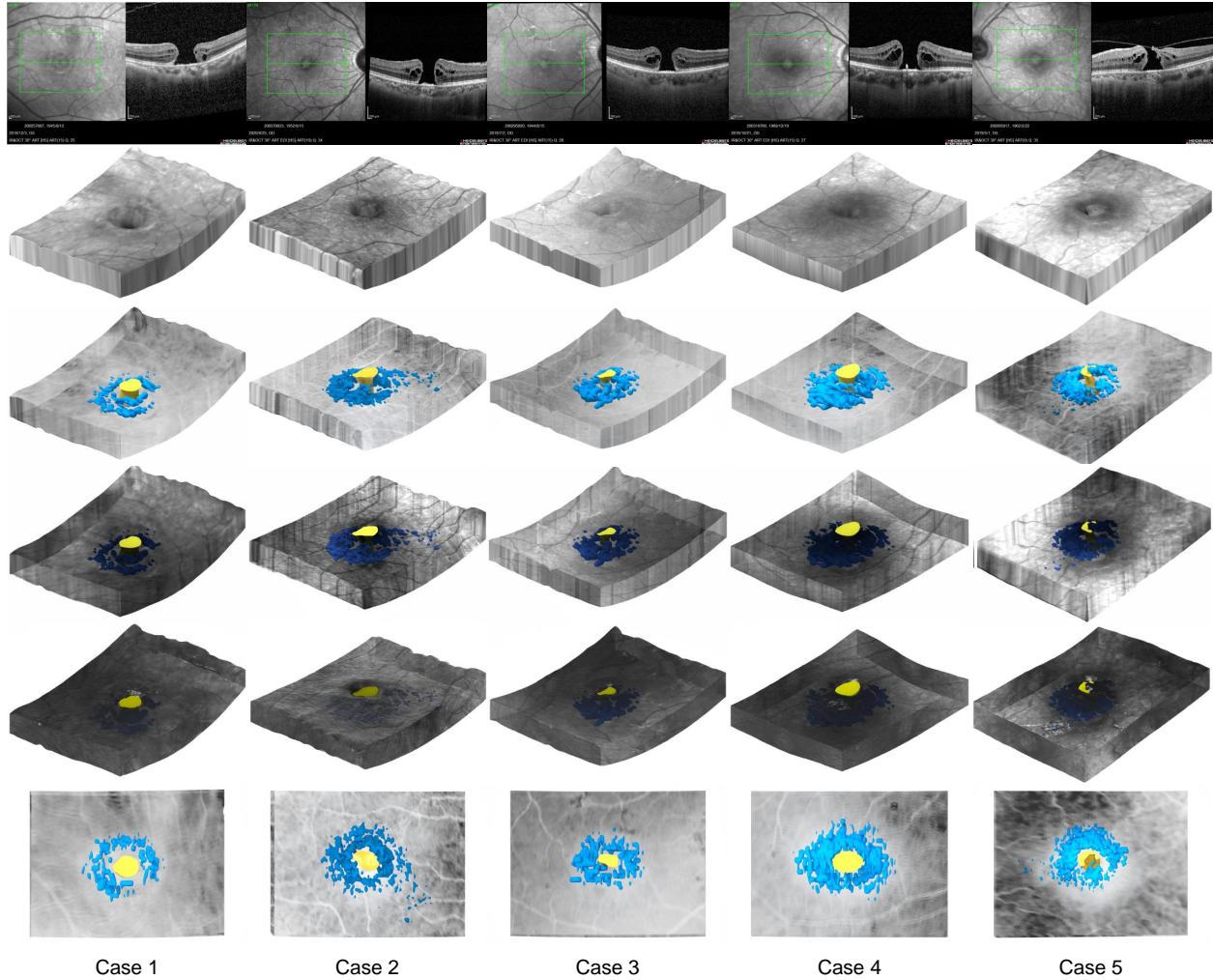


Fig. 14: Displayed are five cases with their original images and reconstruction outcomes. The first row presents the pre-segmentation original images for each case. Rows two to five show the reconstructions based on five different grid arrangements, while the sixth row provides a top-view of the reconstruction results. Within the reconstructions, yellow regions indicate macular holes and green regions signify macular edema.

Central circle: Centered on the central depression (macula center), with a diameter of 1 **optic disc** (The optic disc represents a modestly elevated, circular or elliptical region located on the retina of the eyeball, playing an indispensable role in the diagnosis and management of a spectrum of ophthalmic disorders. Clinicians frequently utilize the diameter of the optic disc as a benchmark. In most cases, 1 optic disc is equivalent to 1 millimeter. Within ophthalmic practice, this metric often serves as a convenient unit to describe the extent of pathological changes on the retina.). This area is also referred to as the "central zone" or "macular zone".

Intermediate circle: Still centered on the central depression but with a diameter of 3 optic discs. This circle surrounds the central circle, with a width of 1 optic disc. This area is also referred to as the "inner circle" or "intermediate zone".

Outer circle: Also centered on the central depression, with a diameter of 6 optic discs. This circle surrounds the intermediate circle, also with a width of 1 optic disc. This area is called the "outer circle" or "peripheral zone".

Clinical doctors can use these regions to more precisely de-

scribe the location and severity of lesions, thereby predicting potential visual problems and developing appropriate treatment strategies. For example, lesions in the macula center (F region) may require emergency intervention to prevent further visual impairment. While peripheral zone lesions may not require immediate treatment, they should be monitored continuously to prevent spread to critical areas.

Therefore, the quantitative indicators provided by the ETDRS grid have extremely high guidance value in clinical practice. After completing retinal fundus 3D reconstruction, we based the ETDRS grid on the established model for regional division and calculated the volume of the retina, macular hole, and macular edema in each region and circle. This allows doctors to judge the severity of the macular hole based on the quantitative data of various regions and provides a reference for selecting treatment programs, which is of great clinical significance.

Specifically, the operation process is as follows: First, as shown in Fig.15(b), scale the ETDRS grid to match the reconstructed ocular structure, ensuring that they are adjusted in size

Table 7: Diagram depicting volume calculations for different sections according to the ETDRS zoning chart, and the volumes inside the intermediate circle and the Outer Circle, where IC is the Intermediate Circle (diameter of 3mm), OC is the outer circle (diameter of 6mm), MH is the Macular Hole, ME is the Macular Edema, RA is the Retina. These five cases correspond to the examples in Fig.14.

MH										
	IC	OC	F	IN	IT	IS	II	ON	OS	OI
Case 1	0.056	0.056	0.056	0.000	0.000	0.000	0.000	0.000	0.000	0.000
Case 2	0.035	0.035	0.035	0.000	0.000	0.000	0.000	0.000	0.000	0.000
Case 3	0.020	0.020	0.020	0.000	0.000	0.000	0.000	0.000	0.000	0.000
Case 4	0.067	0.067	0.067	0.000	0.000	0.000	0.000	0.000	0.000	0.000
Case 5	0.033	0.033	0.033	0.000	0.000	0.000	0.000	0.000	0.000	0.000

ME										
	IC	OC	F	IN	IT	IS	II	ON	OS	OI
Case 1	0.066	0.066	0.003	0.015	0.021	0.015	0.012	0.000	0.000	0.000
Case 2	0.155	0.158	0.022	0.045	0.030	0.011	0.047	0.000	0.001	0.003
Case 3	0.088	0.088	0.017	0.031	0.020	0.006	0.016	0.000	0.000	0.000
Case 4	0.246	0.247	0.013	0.099	0.051	0.020	0.062	0.001	0.000	0.000
Case 5	0.143	0.144	0.012	0.023	0.042	0.004	0.062	0.000	0.000	0.001

RA										
	IC	OC	F	IN	IT	IS	II	ON	OS	OI
Case 1	2.213	7.132	0.172	0.492	0.536	0.505	0.509	1.450	0.958	1.556
Case 2	2.521	7.596	0.254	0.557	0.582	0.560	0.568	1.488	0.988	1.667
Case 3	2.393	7.213	0.257	0.535	0.544	0.526	0.532	1.433	0.936	1.520
Case 4	2.690	7.776	0.254	0.632	0.612	0.569	0.623	1.529	0.969	1.596
Case 5	2.454	7.386	0.248	0.516	0.588	0.533	0.570	1.410	0.906	1.691

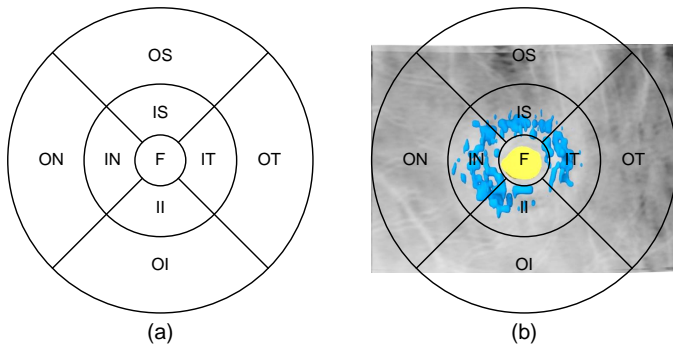


Fig. 15: The ETDRS grid is shown as (a), which contains 9 sectors: F (Foveal), IS (Inner Superior), II (Inner Inferior), IT (Inner Temporal), IN (Inner Nasal), OS (Outer Superior), OI (Outer Inferior), OT (Outer Temporal), ON (Outer Nasal); and three concentric circles: central circle, intermediate circle, outer circle. (b) represents the schematic diagram of the ETDRS superimposed on the reconstructed retina after proportional scaling.

according to the actual physical space ratio. Then superimpose them by taking the macula as the center. On this basis, we separately calculate the volume of the macular retina, the macular hole, and the macular edema in each ETDRS region and within each concentric circle. Table.7 summarizes the calculation results of the five examples in Fig.14.

5. Clinical impact

In this study, our task was to develop a macular hole and retinal fundus 3D reconstruction method that can be used clinically. Model segmentation is the foundation of the task, so we proposed the DEFN model, which has excellent performance in segmenting the macular hole and the retinal components. On this basis, we realized high-precision 3D reconstruction of ocular structures, providing more possibilities for clinical application. Unlike most previous studies, our work not only made

progress in algorithms but also focused on actual clinical application requirements. For example, most previous studies generally only focused on the accuracy of image segmentation, while this study further considered surgical decision-making and disease prediction, thus having higher clinical application value. The core contribution of this study is to provide highly precise three-dimensional views and quantitative indicators for doctors in the surgical decision-making process, which not only optimizes surgical programs but also allows data-based prediction and evaluation of treatment effects in the postoperative stage. For the macular hole, common treatment methods include vitrectomy surgery, which usually involves the injection of silicone oil or sulfur hexafluoride (C3F8) filler during surgery. Using the excellent segmentation capabilities of the DEFN model and high-precision 3D reconstruction in this study, doctors can accurately understand the volume and precise location of the macular hole through quantitative 3D reconstruction data before vitrectomy. This is crucial for determining the type and amount of filler, as the volume of the macular hole directly affects the amount of filler required. During surgery, high-definition 3D images can provide doctors with clear and intuitive three-dimensional views to help them perform surgical steps more precisely. Postoperatively, quantitative indicators for the macular hole can also be used to monitor disease recovery progress and evaluate treatment effects, such as by monitoring the stability of silicone oil or C3F8, allowing doctors and patients to more accurately understand the postoperative recovery situation and potential need for drug treatment.

In summary, this study not only developed a model with excellent segmentation effects that can better segment the macular hole and the macular edema on the retina but also performed 3D reconstruction based on the segmentation results and quantified various indicators in conjunction with clinical practice, providing strong support for clinical practice, including but not limited to diagnosis, surgery, and postoperative monitoring. Furthermore, through appropriate fine-tuning, DEFN has the potential to extend its application to other complex retinal diseases such as macular degeneration or retinal detachment, providing clinicians with more comprehensive solutions.

6. Conclusions

Macular diseases are difficult-to-treat ocular diseases with millions of new cases each year, mainly involving the macular area of the retina and causing a sharp decline in central vision and visual field loss. Without timely treatment, it may further develop into irreversible vision loss, seriously affecting patients' visual function and quality of life. Accurate diagnosis and understanding of the spatial status are important for selecting and implementing treatment plans in the treatment of the macular hole. However, segmenting the macular hole faces multiple challenges: First, due to the scarcity of samples, data-driven methods find it difficult to ensure accuracy. Second, interference from retinal edges and vitreous opacities will affect the quality of imaging, and the similarity between the macular hole and retinal fluid all increase the complexity of segmentation and 3D reconstruction. To address these challenges, we developed DEFN, a 3D segmentation model for features like the

macular hole that are less obvious and difficult to segment accurately. The model contains three modules: FuGH, S3DSA, and HSE, mainly used for feature enhancement, data augmentation, and noise removal. It was trained and tested using the data augmentation technique SRDI and large annotated datasets ROME-3914 and CARS-30k and finally adopted a novel network optimization technique DWC. In the experiment compared with 13 baselines, the Dice score of our model using the isolated macular hole injection method in the macular hole category was 1.73% higher than that of the best baseline, and the HD in the macular hole category was 26.01, which also below the optimal baseline of 30.05. The data show that our study significantly improved the accuracy and robustness of the macular hole segmentation, with excellent performance in region segmentation, boundary segmentation, and detail processing. We also provided a novel 3D structural reconstruction scheme that can achieve precise ocular structural 3D reconstruction in 33s and provide quantifiable indicators, which can be widely applied clinically. Our study not only achieved a new technical level in the macular hole segmentation but also provided doctors with unprecedented decision support tools through real-time, high-precision 3D reconstruction and parameter quantification, with the potential to fundamentally change the diagnosis and treatment of difficult macular diseases.

Acknowledgements

This research is supported in part by the National Natural Science Foundation of China (No. 62206242).

References

- Alalwan, N., Abozeid, A., ElHabshy, A.A., Alzahrani, A., 2021. Efficient 3d deep learning model for medical image semantic segmentation. *Alexandria Engineering Journal* 60, 1231–1239.
- Bai, F., Marques, M.J., Gibson, S.J., 2017. Cystoid macular edema segmentation of optical coherence tomography images using fully convolutional neural networks and fully connected crfs. *arXiv preprint arXiv:1709.05324*.
- Çiçek, Ö., Abdulkadir, A., Lienkamp, S.S., Brox, T., Ronneberger, O., 2016. 3d u-net: learning dense volumetric segmentation from sparse annotation, in: *Medical Image Computing and Computer-Assisted Intervention—MICCAI 2016: 19th International Conference, Athens, Greece, October 17–21, 2016, Proceedings, Part II* 19, Springer. pp. 424–432.
- Coleman, A.L., Yu, F., Ensrud, K.E., Stone, K.L., Cauley, J.A., Pedula, K.L., Hochberg, M.C., Mangione, C.M., 2010. Impact of age-related macular degeneration on vision-specific quality of life: Follow-up from the 10-year and 15-year visits of the study of osteoporotic fractures. *American journal of ophthalmology* 150, 683–691.
- Dai, W., Woo, B., Liu, S., Marques, M., Engstrom, C., Greer, P.B., Crozier, S., Dowling, J.A., Chandra, S.S., 2022. Can3d: Fast 3d medical image segmentation via compact context aggregation. *Medical Image Analysis* 82, 102562.
- Guo, Y., Hormel, T.T., Xiong, H., Wang, J., Hwang, T.S., Jia, Y., 2020. Automated segmentation of retinal fluid volumes from structural and angiographic optical coherence tomography using deep learning. *Translational vision science & technology* 9, 54–54.
- Hatamizadeh, A., Nath, V., Tang, Y., Yang, D., Roth, H.R., Xu, D., 2021. Swin unetr: Swin transformers for semantic segmentation of brain tumors in mri images, in: *International MICCAI Brainlesion Workshop*, Springer. pp. 272–284.
- Hatamizadeh, A., Tang, Y., Nath, V., Yang, D., Myronenko, A., Landman, B., Roth, H.R., Xu, D., 2022. Unetr: Transformers for 3d medical image segmentation, in: *Proceedings of the IEEE/CVF winter conference on applications of computer vision*, pp. 574–584.
- He, Y., Carass, A., Liu, Y., Jedynek, B.M., Solomon, S.D., Saidha, S., Calabresi, P.A., Prince, J.L., 2021. Structured layer surface segmentation for retina oct using fully convolutional regression networks. *Medical image analysis* 68, 101856.
- Hu, J., Chen, Y., Yi, Z., 2019. Automated segmentation of macular edema in oct using deep neural networks. *Medical image analysis* 55, 216–227.
- Hu, J., Shen, L., Sun, G., 2018. Squeeze-and-excitation networks, in: *Proceedings of the IEEE conference on computer vision and pattern recognition*, pp. 7132–7141.
- Huang, X., Bajaj, R., Li, Y., Ye, X., Lin, J., Pugliese, F., Ramasamy, A., Gu, Y., Wang, Y., Torii, R., et al., 2023. Post-ivus: A perceptual organisation-aware selective transformer framework for intravascular ultrasound segmentation. *Medical Image Analysis* 89, 102922.
- Huang, X., Yao, C., Xu, F., Chen, L., Wang, H., Chen, X., Ye, J., Wang, Y., 2022. Mac-resnet: Knowledge distillation based lightweight multiscale-attention-crop-resnet for eyelid tumors detection and classification. *Journal of Personalized Medicine* 13, 89.
- Ibtehaz, N., Rahman, M.S., 2020. Multiresunet: Rethinking the u-net architecture for multimodal biomedical image segmentation. *Neural networks* 121, 74–87.
- Isensee, F., Jaeger, P.F., Kohl, S.A., Petersen, J., Maier-Hein, K.H., 2021. nnu-net: a self-configuring method for deep learning-based biomedical image segmentation. *Nature methods* 18, 203–211.
- Jaderberg, M., Simonyan, K., Zisserman, A., et al., 2015. Spatial transformer networks. *Advances in neural information processing systems* 28.
- Kamnitsas, K., Ledig, C., Newcombe, V.F., Simpson, J.P., Kane, A.D., Menon, D.K., Rueckert, D., Glocker, B., 2017. Efficient multi-scale 3d cnn with fully connected crf for accurate brain lesion segmentation. *Medical image analysis* 36, 61–78.
- Kervadec, H., Bouchtiba, J., Desrosiers, C., Granger, E., Dolz, J., Ayed, I.B., 2019. Boundary loss for highly unbalanced segmentation, in: *International conference on medical imaging with deep learning*, PMLR. pp. 285–296.
- Krizhevsky, A., Sutskever, I., Hinton, G.E., 2012. Imagenet classification with deep convolutional neural networks. *Advances in neural information processing systems* 25.
- Kugelman, J., Caneiro, D.A., Read, S.A., Vincent, S.J., Collins, M.J., 2023. Enhanced oct chorio-retinal segmentation in low-data settings with semi-supervised gan augmentation using cross-localisation. *Computer Vision and Image Understanding*, 103852.
- LaLonde, R., Bağcı, U., 2018. Capsules for object segmentation. *arXiv preprint arXiv:1804.04241*.
- Lee, H.H., Bao, S., Huo, Y., Landman, B.A., 2022. 3d ux-net: A large kernel volumetric convnet modernizing hierarchical transformer for medical image segmentation. *arXiv preprint arXiv:2209.15076*.
- Li, W., Wang, G., Fidon, L., Ourselin, S., Cardoso, M.J., Vercauteren, T., 2017. On the compactness, efficiency, and representation of 3d convolutional networks: brain parcellation as a pretext task, in: *Information Processing in Medical Imaging: 25th International Conference, IPMI 2017, Boone, NC, USA, June 25–30, 2017, Proceedings* 25, Springer. pp. 348–360.
- Lin, J., Huang, X., Zhou, H., Wang, Y., Zhang, Q., 2023. Stimulus-guided adaptive transformer network for retinal blood vessel segmentation in fundus images. *Medical Image Analysis* 89, 102929.
- Lin, S., Liu, N., Nazemi, M., Li, H., Ding, C., Wang, Y., Pedram, M., 2018. Fft-based deep learning deployment in embedded systems, in: *2018 Design, Automation & Test in Europe Conference & Exhibition (DATE)*, IEEE. pp. 1045–1050.
- Lin, T.Y., Goyal, P., Girshick, R., He, K., Dollár, P., 2017. Focal loss for dense object detection, in: *Proceedings of the IEEE international conference on computer vision*, pp. 2980–2988.
- Liu, B., Ding, Y., Jiao, J., Ji, X., Ye, Q., 2021. Anti-aliasing semantic reconstruction for few-shot semantic segmentation, in: *Proceedings of the IEEE/CVF conference on computer vision and pattern recognition*, pp. 9747–9756.
- Loshchilov, I., Hutter, F., 2017. Decoupled weight decay regularization. *arXiv preprint arXiv:1711.05101*.
- Milletari, F., Navab, N., Ahmadi, S.A., 2016. V-net: Fully convolutional neural networks for volumetric medical image segmentation, in: *2016 fourth international conference on 3D vision (3DV)*, Ieee. pp. 565–571.
- Morano, J., Hervella, Á.S., Barreira, N., Novo, J., Rouco, J., 2020. Multimodal transfer learning-based approaches for retinal vascular segmentation. *arXiv preprint arXiv:2012.10160*.
- Myronenko, A., 2019. 3d mri brain tumor segmentation using autoencoder reg-

- ularization, in: *Brainlesion: Glioma, Multiple Sclerosis, Stroke and Traumatic Brain Injuries: 4th International Workshop, BrainLes 2018, Held in Conjunction with MICCAI 2018, Granada, Spain, September 16, 2018, Revised Selected Papers, Part II 4*, Springer. pp. 311–320.
- Niyas, S., Pawan, S., Kumar, M.A., Rajan, J., 2022. Medical image segmentation with 3d convolutional neural networks: A survey. *Neurocomputing* 493, 397–413.
- Wang, R., Chen, S., Ji, C., Fan, J., Li, Y., 2022. Boundary-aware context neural network for medical image segmentation. *Medical Image Analysis* 78, 102395.
- Wang, W., Chen, C., Ding, M., Yu, H., Zha, S., Li, J., 2021. Transbts: Multimodal brain tumor segmentation using transformer, in: *Medical Image Computing and Computer Assisted Intervention–MICCAI 2021: 24th International Conference, Strasbourg, France, September 27–October 1, 2021, Proceedings, Part I 24*, Springer. pp. 109–119.
- Xia, L., Zhang, H., Wu, Y., Song, R., Ma, Y., Mou, L., Liu, J., Xie, Y., Ma, M., Zhao, Y., 2022. 3d vessel-like structure segmentation in medical images by an edge-reinforced network. *Medical Image Analysis* 82, 102581.
- Xu, W., Liu, H., Wang, X., Qian, Y., 2019. Liver segmentation in ct based on resunet with 3d probabilistic and geometric post process, in: *2019 IEEE 4th International Conference on Signal and Image Processing (ICSIP)*, IEEE. pp. 685–689.
- Yang, D., Xiong, T., Xu, D., Zhou, S.K., Chen, M., Zhoubing, X., Comaniciu, D., Park, J.h., 2019. Deep image-to-image recurrent network with shape basis for automatic vertebra labeling in large-scale 3d ct volumes. US Patent 10,366,491.
- Yeung, M., Sala, E., Schönlieb, C.B., Rundo, L., 2022. Unified focal loss: Generalising dice and cross entropy-based losses to handle class imbalanced medical image segmentation. *Computerized Medical Imaging and Graphics* 95, 102026.
- Zhang, S., Xi, F., Chen, S., Zhang, Y.D., Liu, Z., 2015. Segment-sliding reconstruction of pulsed radar echoes with sub-nyquist sampling. arXiv preprint arXiv:1503.00434 .
- Zhang, Z., Liu, Q., Wang, Y., 2018. Road extraction by deep residual u-net. *IEEE Geoscience and Remote Sensing Letters* 15, 749–753.
- Zhou, H.Y., Guo, J., Zhang, Y., Yu, L., Wang, L., Yu, Y., 2021. nn-former: Interleaved transformer for volumetric segmentation. arXiv preprint arXiv:2109.03201 .